Stony Brook University

Development of a Line-scanned Dual-axis Confocal Microscope for Video-rate Diagnostic Imaging

A Dissertation Presented

by

Danni Wang

to

The Graduate School

in Partial Fulfillment of the

Requirements

for the Degree of

Doctor of Philosophy

in

Biomedical Engineering

Stony Brook University

December 2014

Stony Brook University

The Graduate School

Danni Wang

We, the dissertation committee for the above candidate for the

Doctor of Philosophy degree, hereby recommend

acceptance of this dissertation.

Jonathan T.C. Liu, Ph.D.
Assistant Professor, Department of Mechanical Engineering
University of Washington

Yingtian Pan, Ph.D.
Professor, Department of Biomedical Engineering
Stony Brook University

Emilia Entcheva, Ph.D.
Professor, Department of Biomedical Engineering
Stony Brook University

Thomas Weinacht, Ph.D.
Professor, Department of Physics
Stony Brook University

This dissertation is accepted by the Graduate School

Charles Taber

Dean of the Graduate School

Abstract of the Dissertation

Development of a Line-scanned Dual-axis Confocal Microscope for Video-rate Diagnostic Imaging

by

Danni Wang

Doctor of Philosophy

in

Biomedical Engineering

Stony Brook University

2014

The prevalence of oral cancer has been increasing at an alarming rate in recent years. Due to a limited understanding of the cause and progression of this disease, patient prognosis remain poor, and the mortality and morbidity of the disease remain significant. The need to diagnose cancerous regions early is key to patient survival. However, the high cost and invasive nature of standard pathological analysis motivates the search for an alternative real-time imaging technology that provides accurate non-invasive early diagnosis of the disease. The goal of this thesis is to develop a line-scanned dual-axis confocal (LS-DAC) microscope for high-resolution, high-contrast, high-speed imaging suitable for real-time non-invasive clinical diagnoses. The performance of the LS-DAC microscope architecture is characterized by measuring its axial and lateral response in water as well as a homogeneous scattering phantom (Intralipid). The accuracy of the results are assessed and confirmed by comparison with results from a Monte Carlo scattering simulation of the system. In addition, a parallel comparison between the LS-DAC and our existing point-scanned dual-axis confocal (PS-DAC) microscope is performed to ensure comparable imaging quality at shallow depths. Furthermore, a heterogeneous phantom has been developed and a deconvolution algorithm utilized to aid the characterization and contrast enhancement of the DAC setup, respectively. Finally, the performance of the LS-DAC is demonstrated by imaging *ex vivo* and *in vivo* biological samples in fluorescence mode. The tabletop LS-DAC developed in this thesis research serves as a basic prototype and benchmark system for a miniaturized portable LS-DAC that is also being developed in our lab for affordable non-invasive, real-time diagnostic purposes in patients.

I dedicate this thesis to my beloved grandfather and late-grandmother.
I hope I've made you proud.

“We are all stories, in the end. Just make it a good one.”

– The Doctor

Table of Contents

List of Figures

List of Tables

List of Abbreviations

CCD	Charge-coupled device
DAC	Dual-axis confocal
FITC	Fluorescein isothiocyanate
FOV	Field-of-view
FPS	Frames-per-second
FWHM	Full-width at half-max
LS-	Line-scanned
NA	Numerical Aperture
PMT	Photomultiplier Tube
PS-	Point-scanned
PSF	Point-spread function
SAC	Single-axis confocal
SBR	Signal-to-background Ratio
sCMOS	Scientific complementary metal–oxide–semiconductor
SIL	Solid immersion lens
SS-DAC	Sheet-scanned dual-axis confocal
WD	Working distance

Acknowledgments

First and foremost, I would like to express my deepest gratitude towards my advisor Dr. Jonathan Liu, without whom all this work would not have been possible. Thank you for taking me under your wings and training me to not only become a better scientist but also a better person. Sorry for the extra gray hairs.

To my dissertation committee members: Dr. Yingtian Pan, Dr. Emilia Entcheva, and Dr. Thomas Weinacht, thank you for introducing me to and guiding me through parts of the marvelous world of optics.

To all of the Liu lab members I have had the pleasure of working with over the past few years, you have been very special. To Steve (my lab-partner-in-crime for the past 4 years) in particular, thanks for the laughs and for always keeping me on my toes.

To our brilliant collaborators, namely Dr. Milind Rajadhyaksha and Dr. Michael Mandella, thank you for the very helpful insights and discussions over coffee and email.

To my "academic cousins", Dr. Christopher Hoy and Dr. Christopher Glazowski, thank you for all the helpful comments, nerdy discussions, and encouragements at conferences and over the internet.

To Dr. Poul-Erik Lindelof, thank you for all of the LEGO sets in my childhood; they are partially responsible for my choice in becoming an engineer instead of a pianist.

I would also like to thank my wonderful friends from all over the world for picking up the phone at odd hours of the night to talk to me. Thank you for keeping me smiling, for reminding me to eat and sleep (or in general to retain some sort of semblance of normality in life), and for adding the necessary doses of sarcasm, wit, humor, reality check, and wisdom to my chaotic life. You know who you are. You are a right bunch of weirdoes and I love you all.

To my boyfriend Johan, I am truly grateful to have found you. Thank you for all the amazing adventures we have had and I look forward to the ones to come.

Last but certainly not least, to my parents, thank you for your love and support over the years in perhaps more ways than I deserve. I know I have never been one to accept all the rules and it must have been tough watching me grow up, but hopefully the apple has at least fallen on the same Hemisphere as the tree.

Chapter 1. Background and introduction

1.1 Oral cancer

Oral cancer is the sixth leading malignancy in the world. With approximately 50,000 new cases annually, oral cancer comprises ~3% of all neoplasia diagnosed in the U.S. The poor 5-year survival rate (~57%) in combination with the projected death rate in 2012 of ~1.2 death per hour in newly diagnosed patients (~450,000 cases per year) makes oral cancer a particularly challenging disease. More than 90% of oral cancers are categorized as squamous cell carcinomas (SCC) and are primarily located on the tongue, lips, and floor of the mouth[6-8]. In early stages of this disease, the dysplastic regions are difficult to detect. If not detected early, the precancerous lesions can quickly take on an aggressive metastatic route and spread through the submandibular, cervical, or jugular lymphatic pathways to the distal organs, such as the lungs. Furthermore, as the disease progresses, oral sub-mucosal fibrosis occurs. This reduces the patient's oral opening capacity and thereby their ability to masticate, speak, and swallow, which increases the difficulty for the physician to access the region of interest and make a proper diagnosis[9]. Due to the elusive nature of the disease in its early stage in combination with the aggressive nature of its metastasis, early detection is the key to patient survival.

1.2 Histopathology and other diagnostic tools

Histopathology remains the gold standard for general cancer diagnostics, in which samples of interest are extensively processed (fixing, sectioning, staining) before they are examined under a microscope. By studying the often subtle structural changes in the lesion microenvironment not visible to the naked-eye, pathologists can determine the tissue status with high sensitivity and specificity. However, histopathology is a highly inefficient, costly and invasive procedure, which is often not readily available to all physicians; therefore, adjunctive diagnostic tools have been explored. Current techniques that have been tested in the dental clinic for their efficacy include: oral brush biopsy, toluidine blue staining, chemiluminescence imaging, and autofluorescence imaging.

Oral brush biopsy is a less invasive alternative to regular histopathology. Using a commercially available kit (OralScan™ Laboratories Inc. Suffern, NY), a small biopsy sample containing epithelial layers of the lesion is taken and sent to the pathology lab for analysis. This procedure can be attractive to patients not willing to be subjected to scalpel biopsies; however, there is a high false negative rate due to improper sampling of the lesions, making the procedure less than ideal[10].

Toluidine blue (TB) is found to be excellent at differentiating between normal versus abnormal tissues since it stains abnormal oral tissue blue, and the procedure for TB staining is a basic vital rinse, which is non-invasive. Unfortunately, TB is not specific enough to distinguish precancerous lesions from inflammation or regions of tissue trauma, resulting in high rates of false positive diagnosis. The usage is currently limited to in conjunction with the FDA approved Vizilite Plus system (Zila Inc., Phoenix, AZ)[11].

Chemiluminescence relies on the altered nuclear-to-cytoplasmic ratio of precancerous lesions. By dehydrating the lesions with acetic acid, regions of high nuclear density are highlighted white, indicating the presence of abnormality. The existing data is insufficient to determine the efficacy of the chemiluminescence technique[12].

Some light-based detection techniques have been explored as well:

VELscope (LED Dental Inc., White Rock, BC, Canada) utilizes the change in tissue autofluorescence due to changes in tissue structure, metabolism, and other subcellular details to distinguish normal and abnormal oral tissue. A lesion is considered negative if it retained its natural autofluorescence, and considered positive if the autofluorescence is lost. However, autofluorescence was found to be insufficient to provide diagnostic information with high specificity[13-15].

A reflectance optical spectroscope, Identafi®, has recently entered its clinical study stage[16]. This device uses both the tissue reflectance and autofluorescence in combination with amber-green light (545 nm) visualization of keratinization and vascularity of suspicious lesions. This technology is still in its clinical infancy and although initially successful, more data would need to be obtained to assess the viability of Identafi® as a diagnostic tool for oral cancer[8].

Biomarker-based blood and saliva testing are also being developed to specifically detect changes in cellular DNA, mRNA transcript, altered protein level, etc.[17-19]. While minimally invasive, these technologies are also still in their infancy and have yielded fairly inconclusive results[8].

Name	Clinical use	Drawback	Recommendation
Histopathology	Microscopic analysis of biopsy samples	Time consuming. Expensive. Invasive.	Current gold standard
Brush biopsy	Less invasive biopsy for histopathology analysis.	High false negative due to improper sampling	Not recommended
Toluidine Blue staining	TB staining to distinguish normal from abnormal tissue with high sensitivity	Low specificity	FDA approved with Vizilite, usage limited
Chemiluminescence	Acetic acid stain to highlight regions of high nuclear density	Low specificity	Insufficient clinical data
Autofluorescence	Image tissue autofluorescence to visualize suspicious lesions	Low specificity	FDA approved with VELscope, usage limited
Reflectance spectroscopy	Image tissue reflectance and autofluorescence to visualize suspicious lesions	N/A	Insufficient data
Biomarkers	Measure change in concentration of DNA, mRNA transcript, protein levels in blood or saliva	N/A	Insufficient data

Table 1. Summary of selected oral cancer diagnostics methods

All of the adjunctive diagnostic tools described above have received no recommendation at this time for use as a universal screening tool for oral cancer diagnostics (**Table 1**). Since the underlying causes of oral SCC is highly dependent on the patient's life style, hygiene, diet, and family history, the etiology of the malignancy eludes our full understanding. Nevertheless, there is a desperate need for a technology that allows early detection of the malignancy with high sensitivity and specificity that approaches the gold standard of invasive histopathology. Ideally, the technology will achieve subcellular spatial resolution (<5 μm) and video rate (>10 fps) imaging speed with a millimeter-range working distance.

1.3 Confocal microscopy

Microscopy has been an important part of scientific research for centuries. By studying details normally invisible to the naked eye, important and interesting discoveries have been made. These discoveries have contributed substantially to the fields of pathological diagnostics and disease treatment. In the standard cancer diagnostic paradigm, suspicious lesions are excised from the patient and must be extensively processed before they are examined under a microscope. Despite the time-consuming, invasive and costly nature of this practice, histopathology remains the technique with the best specificity and sensitivity for current cancer diagnosis.

The majority of the diagnostic methods shown in **Table 1** require direct imaging of the region of interest to investigate suspicious lesions, and the most notable drawbacks are low specificity and invasiveness. The wide-field technologies generally provide good sensitivity whereas the microscope adds specificity when used to diagnose suspicious regions; therefore, a microscope that allows for the rapid non-invasive or minimally-invasive assessment of suspicious tissue regions is needed.

1.3.1 Principles of confocal microscopy

The concept of confocal microscopy is to selectively collect only the light from a small focal volume while minimizing the collection of background scattered light from out-of-focus regions. By scanning that focal volume over a sample, we can reconstruct an image (generally one pixel at a time in a conventional point-scanned system). The confocal architecture efficiently rejects out-of-focus and multiply-scattered light providing an imaging resolution and contrast that are superior to conventional wide-field microscopes. An important feature of a confocal microscope is its non-destructive optical sectioning ability – the ability to interrogate subsurface layers of tissue without physically cutting the tissue. In terms of clinical diagnostics, this can potentially provide physicians with a “virtual biopsy” that contains much of the details obtained with a physical biopsy without disrupting the native tissue.

1.3.2 Single-axis and dual-axis confocal microscopy

In conventional confocal microscopes, the illumination and collection lights are coaxial in the tissue (**Fig. 1.3.2a**), in other words, they travel the same paths. Here we refer to this configuration as single-axis confocal (SAC). This configuration utilizes lenses with high numerical aperture (NA) in order to sharply focus the illumination light to a small focal spot. The reflected

or fluorescent light generated at the focal spot is collected by a detection pinhole (in the form of a physical pinhole or an optical fiber). The pinholes serve as spatial filters that reject out-of-focus and multiply scattered light from the sample, thus providing the system with excellent optical sectioning ability. The focus can be scanned through the tissue using raster-scanning or other pattern-scanning methods in order to generate a 2D or 3D image of the area under interrogation.

The working distance (WD) of a single-axis confocal microscope can be defined as:

$$WD = \frac{D}{2(NA)}$$

where *D* is the diameter of the lens focusing the light into the tissue and *NA* is the numerical aperture of the beam. Since *WD* is inversely proportional to *NA*, the working distance of high *NA* focused beams is short; thus, the imaging depth of the system is physically limited to a relatively superficial level (<100 μm depending on specific tissue type). In addition, the short working distance between the lens surface and biological samples forces the scanning of the beams to be done prior to the lens and in turn generates off-axis aberrations that have to be corrected by adding multiple optical elements, which in turn adds to the complexity of the optical design.

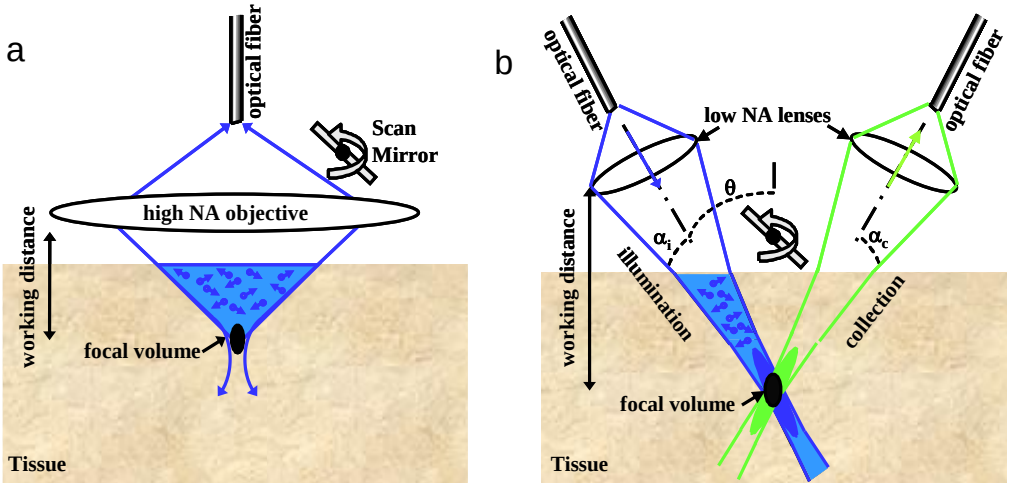

Figure 1.3.2. Single-axis confocal (SAC) and dual-axis confocal (DAC) design configurations[1] a) The single-axis confocal microscope design schematic. Note: short working distance, shallow imaging depth, and pre-objective scanning. b) The dual-axis confocal microscope design schematic.

Note: longer working distance, increased imaging depth, and post-objective scanning

Alternatively, by following the original idea proposed by Koester et al.[20], modifications have been made to the SAC configuration so that the illumination and collection light travel different paths. In the dual-axis configuration, low-NA beams are used for illumination and collection. The illumination and collection paths cross the midline (intersect) at a crossing-angle θ (**Fig. 1.3.2b**). In this configuration, scattered light outside the focal volume is statistically less likely to be collected, resulting in enhanced detection sensitivity and contrast.

The working distance (WD) in this configuration is defined as:

$$WD = \frac{D \cos\theta}{2(NA)}$$

The usage of low-NA focused beams in this configuration creates a longer working distance, which allows for the placement of a scanning mirror after the objectives. This design allows for a larger scanned field of view without scanning-induced aberrations. Furthermore, the ability of the DAC configuration to more effectively reject out-of-focus, back-scattered, and multiply-scattered light allows the system to image more deeply than the equivalent SAC configuration as shown in the simulated axial-response plot (**Fig. 1.3.2c**) based on diffraction theory[1] as well as Monte-Carlo scattering simulations[5].

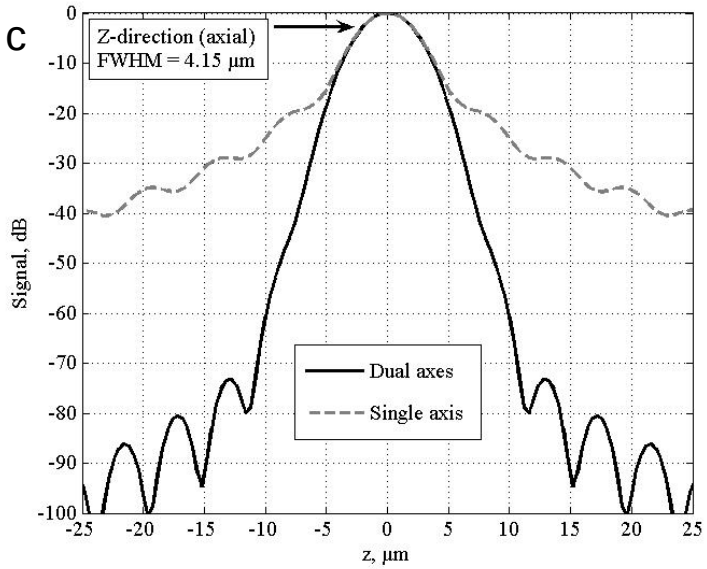

1.3.2c[1]. Theoretical axial responses of the SAC and DAC microscope to a point-reflector. θ =30° and λ =1.3 μm for this particular setup. Note: the microscope setup was configured such that the SAC and DAC would have matching FWHM axial responses.

In order for the microscope to be used in a clinical or surgical setting, the design must be miniaturized. Over the past two decades, numerous efforts have been made to miniaturize the SAC microscope with various degrees of success[21, 22]. Ultimately, the designs aim to balance (with great difficulty) the tradeoff between imaging resolution, contrast, working distance, and field of view. Numerous advancements have also been made by independent groups in the past decade to miniaturize the DAC microscope for clinical use particularly for skin imaging[23-26].

1.3.2.1 Point-scanning

The point-scanned (PS) confocal configuration utilizes scanning mechanisms along two orthogonal axes (typically perpendicular to the optical axis) in order to scan a focal spot through an area of interest to obtain an image in a point-by-point fashion. This configuration offers high imaging resolution and high contrast, but the imaging speed is typically slow, on the order of a

few Hertz. At such slow speeds, the image is highly vulnerable to motion artifacts in clinical settings.

1.3.2.2 Line-scanning

The line-scanned (LS) confocal configuration sacrifices illumination and detection confocality along one dimension to collect signal from an entire line of pixels at once, typically by a camera chip or CCD array. The focal line is scanned through the area of interest and an image is obtained in a line-by-line fashion, thus potentially increasing the imaging speed by n-fold, where n is the number of pixels along the focal line. This configuration sacrifices a modest level of imaging resolution and contrast due to the loss of confocality along one axis[27-31]. However, this configuration is much more resilient against motion artifacts due to its increased imaging frame rate.

1.4 Overarching goal

In this thesis project, we focused on improving the imaging speed of the dual-axis confocal (DAC) imaging system by developing a line-scanned dual-axis confocal (LS-DAC) microscope with comparable imaging performance as an existing PS-DAC microscope (i.e. capable of providing subcellular imaging resolution) at shallow depths in biological tissue.

Chapter 2. Optical design of a Line-scanned Dual-axis Confocal (LS-DAC) system

The development of the dual-axis confocal system has been a steady one since its proof-of-principle study in 2003[32]. Detailed characterization and prototyping have been done to the point-scanned DAC (PS-DAC) for both benchtop[33, 34] as well as miniaturized setups[35, 36]. Different modifications focused on addressing different design parameters of the imaging system including resolution, contrast, and portability. The primary focus of the LS-DAC design is imaging speed. The goal is to be able to image at $\geq$ 10 frames-per-second without significant tradeoffs in imaging resolution and contrast at shallow depths.

2.1 Theory

In the case of the LS-DAC, we expect that when designed correctly, the system spatial resolution along the x-axis (orthogonal to the confocal line) and z-axis (axial) should stay unchanged while the y-axis is expanded into a line and loses confocality along that direction.

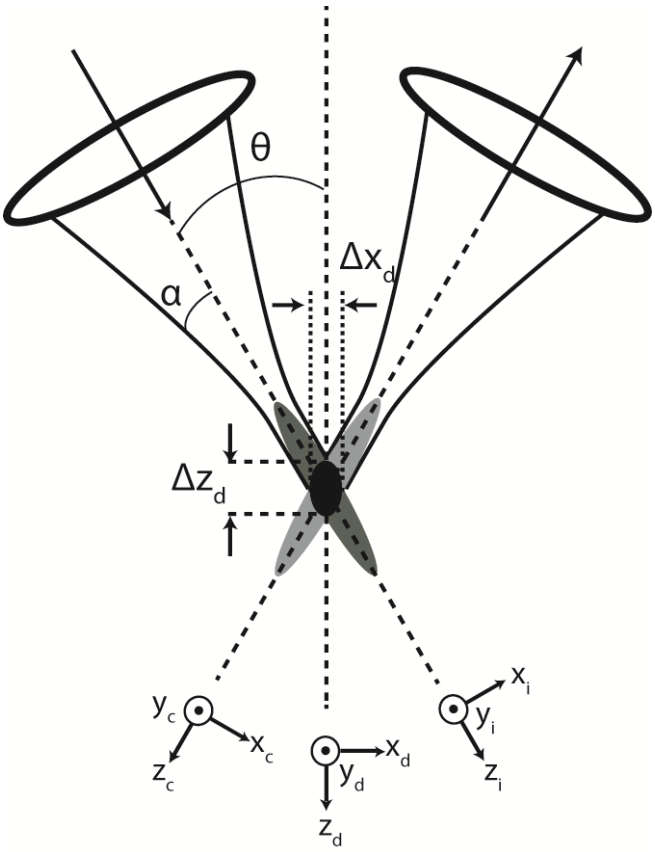

Figure 2.1.1. Schematic of the focal region of the DAC microscope (figure adapted from published work[1])

Consider the focal region of the DAC microscope shown in **Fig 2.1.1**. The main lobe of the point-spread function (PSF) of the illumination path at the focal plane is indicated by the dark gray oval region. Due to the usage of low numerical aperture (NA) objectives, the main lobe has a

narrow transverse dimension and a wide axial dimension. The PSF of the collection path is symmetrically reflected about z_d. The combined PSF of the system is the product of the individual PSFs, indicated as the overlapping region in black.

The illumination and collection coordinates in **Fig 2.1.1** can be expressed in polar coordinates as[1]:

$$\begin{aligned} x_i = x_c = \ x_d \cos\theta - z_d \sin\theta \\ y_c = \ y_c = y_d \\ z_i = z_d \cos\theta + x_d \sin\theta \\ z_c = z_d \cos\theta - x_d \sin\theta \end{aligned} \tag{1}$$

where λ is the wavelength, *n* is the refractive index of the medium, θ is the crossing angle of the dual-axis beams, α is the converging beam angle[32, 37]. Since low-NA lenses are used here, $\sin\alpha \approx \alpha$ for our calculations.

A set of dimensionless coordinates can be defined as a function of the half-angles α_i, and α_c, and wavelengths λ_i, and λ_c (of the illumination and collection beams, respectively):

$$\begin{aligned} v_i = \frac{2\pi}{\lambda_i} n \sqrt{x_i^2 + y_i^2} \sin\alpha_i \\ v_c = \frac{2\pi}{\lambda_c} n \sqrt{x_c^2 + y_c^2} \sin\alpha_c \\ u_i = \frac{2\pi}{\lambda_i} n z_i \, (\sin\alpha_i)^2 \\ u_c = \frac{2\pi}{\lambda_c} n z_c \, (\sin\alpha_c)^2 \end{aligned} \tag{2}$$

The amplitude point spread function (PSF) of the illumination and collection beams are proportional to the integrals[1]:

$$\begin{aligned} U_i(v_i, u_i) \propto \int_0^1 W_i(\rho) J_0(\rho v_i) e^{\frac{-j u_i \rho^2}{2}} \rho d\rho \\ U_c(v_c, u_c) \propto \int_0^1 W_c(\rho) J_0(\rho v_c) e^{\frac{-j u_c \rho^2}{2}} \rho d\rho \end{aligned} \tag{3}$$

W(ρ) is the weighting function used to describe the truncation of the beam. For uniform illumination W(ρ) = 1, and for Gaussian illumination truncated at the $1/e^2$ point, $W(\rho) = e^{-(\frac{\pi\rho}{2})^2}$. J_0 is the zeroth order Bessel function, and ρ is a normalized radial distance variable at the lens aperture.

The overlapping PSF at the focal plane ($u_i = u_c = 0$) is $|U_i U_c|^2$, which is proportional to the detector output V. Under Gaussian illumination, at the focal plane, Eq. (3) can be simplified to yield:

$$U_i(v_i) \propto \int_0^\infty e^{-\left(\frac{\pi\rho}{2}\right)^2} J_0(\rho v_i)\rho d\rho = \frac{2}{\pi^2} e^{-(\frac{v_i}{\pi})^2}$$
$$U_c(v_c) \propto \int_0^\infty e^{-\left(\frac{\pi\rho}{2}\right)^2} J_0(\rho v_c)\rho d\rho = \frac{2}{\pi^2} e^{-(\frac{v_c}{\pi})^2} \quad (4)$$

From which, we obtain:

$$V \propto (\frac{2}{\pi^2} e^{-\left(\frac{v_i}{\pi}\right)^2})(\frac{2}{\pi^2} e^{-\left(\frac{v_c}{\pi}\right)^2}) \quad (5)$$

Substituting Eq. (1) and (2) into (5),

$$V = A[e^{-\frac{8n^2\alpha_i^2}{\lambda_i^2}(x_d^2(\cos\theta)^2 + y_d^2)} e^{-\frac{8n^2\alpha_c^2}{\lambda_c^2}(x_d^2(\cos\theta)^2 + y_d^2)}] \quad (6)$$

where A is a constant. From Eq. (2), we obtain the expression $v^2 = (\frac{2\pi}{\lambda} n)^2 (x^2 + y^2)(\sin\ \alpha)^2 = [\frac{n\alpha}{2\lambda}(x_d \cos\theta + y_d)]^2$, and we thereby obtain the simplified expression

$$V = B(e^{-8v^2})^2 \quad (7)$$

B is a constant. We plot the non-constant portion of Eqn. (7)

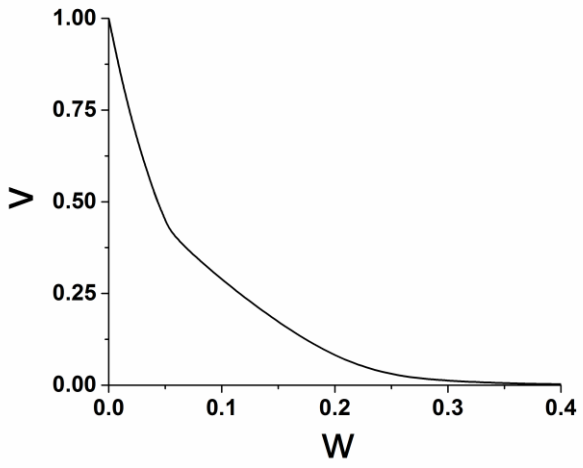

We can find the value of v^2 when V is at 50% of the maximum, $v^2 = 0.0433$. We can thereby solve for the full-width-at-half-maximum (FWHM) lateral resolution x_d at the focus ($y_d = 0$):

$$\Delta x_d = \frac{0.416\lambda}{n\alpha \cos\theta} \quad (8)$$

Similarly, we can calculate the axial response. We start with eq. (3) for (v_i = v_c = 0), and obtain the expression:

$$U_i(u_i) \propto \int_0^\infty e^{-\left(\frac{\pi\rho}{2}\right)^2} e^{\frac{-ju_i\rho^2}{2}} \rho d\rho$$
$$U_c(u_c) \propto \int_0^\infty e^{-\left(\frac{\pi\rho}{2}\right)^2} e^{\frac{-ju_c\rho^2}{2}} \rho d\rho \quad (9)$$

We can express the output V as:

$$V = Ae^{-[8n^2 z_d^2 (\sin\theta)^2 (\frac{\alpha_i^2}{\lambda_i^2} + \frac{\alpha_c^2}{\lambda_c^2})]} \quad (10)$$

And the axial resolution can be solved as:

$$\Delta z_d = \frac{0.416\lambda}{n\alpha \sin\theta} \quad (11)$$

By design, the axial resolution of the DAC microscope is proportional to 1/NA instead of $1/(NA)^2$ for a SAC microscope, allowing us to utilize low-NA optics without significantly sacrificing axial resolution[32].

The most accurate values for the theoretical resolutions of the DAC setup are shown in eqs. (8) and (11). For Gaussian beams truncated at 99% points, the resolution of the LS-DAC in the lateral-x and axial-z directions are 12% larger than the theoretical calculation, as verified by previous publication[1]:

$$\Delta x_d = \frac{0.466\lambda}{n\alpha \cos\theta}, \qquad \Delta z_d = \frac{0.466\lambda}{n\alpha \sin\theta} \quad (12)$$

The samples imaged on the DAC microscope are placed on a fused-silica hemispheric lens, otherwise known as a solid-immersion lens (SIL). The inclusion of the SIL provides several advantages[1]:

1. The curved surface of the hemisphere provides a normal incident interface to minimize off-axis aberrations at the air-glass interface
2. The wave-front curvature of the focused beams is matched to the curved surface of the SIL, which in turn minimizes spherical aberrations when the beam is stationary.
3. The effective NA of the beams is boosted by a factor of the refractive index of the fused-silica (~1.46).
4. The refractive index of fused-silica is similar to biological tissues, making it a convenient and practical index-matching sample stage.

So for our setup using a 658-nm diode laser, 30° crossing angle (θ), and α = 0.21 radians, the theoretical resolutions in air are Δx_d ~ 1.2 μm, and Δz_d ~ 2.1 μm.

Figure 2.1.2 shows the optical setup used to generate the confocal line.

The collimating lens (f = 20 mm) expands the point source (N.A. of the single-mode fiber = 0.11) of light such that the beam radius at the collimated region is 2.2mm. (Calculation follows that NA = n sin θ ≈ n * beam radius/f). A negative cylindrical lens with focal length of 50 mm expands the beam in one dimension only (astigmatism) so that the focusing lens causes the beam to focus in one dimension first before focusing in the other dimension. We utilize the focal line generated at the first imaging plane.

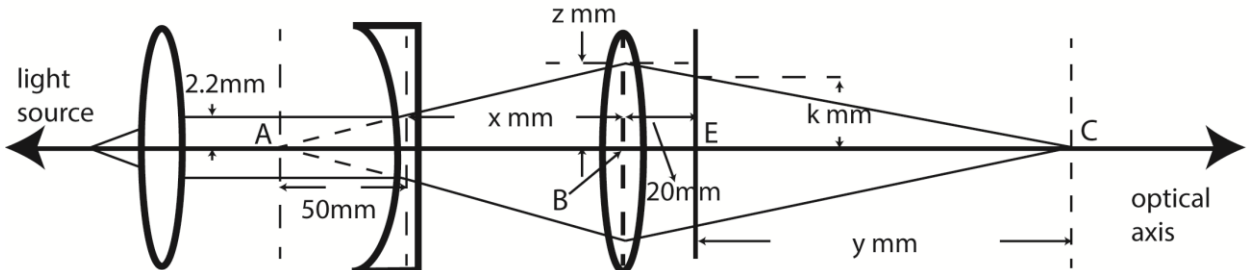

Figure 2.1.2. Schematic drawing of the illumination arm for geometric ray tracing.

Using basic geometrical optics and thin lens approximations, we can establish

$$\frac{1}{\overline{AB}} + \frac{1}{\overline{BC}} = \frac{1}{\overline{BE}}$$
$$\therefore \frac{1}{(50+x)} + \frac{1}{(20+y)} = \frac{1}{20} \quad (13)$$

By the properties of similar triangles, we can establish

$$\frac{f_{cylindrical}}{\overline{AB}} = \frac{2.2}{z} \;\; and \;\; \frac{\overline{CE}}{\overline{BC}} = \frac{k}{z}$$
$$\therefore \frac{50}{(50+x)} = \frac{2.2}{z} \;\; and \;\; \frac{y}{(20+y)} = \frac{k}{z} \quad (14)$$

We can combine (13) and (14) and express *k* as

$$k = 0.88\, mm \quad (15)$$

By varying *x* over the physically accessible locations on the illumination path of our benchtop system (i.e. 10 – 35 mm), *y* varies per equation (13). The line-length (2 times k) is invariant of *x* and *y*. The line-length is adjusted to take into consideration of the SIL, which de-magnifies the line by a factor of 1.46 at the sample. In addition, the calculated line length corresponds to the $1/e^2$ line length, which is 1.699 times the FWHM line-length, which is calculated to be ~650 μm.

2.2 Modeling

Diffraction-based software modeling of the LS-DAC system was performed in ZEMAX (Redmond, WA) to verify the analytical calculations. Monte-Carlo scattering simulations were performed in FRED (Photon Engineering, Tucson, AZ) to gain an understanding of how the system behaves in a homogeneous scattering medium at various imaging depths. Both Monte-Carlo scattering simulations and optical ray-tracing in ZEMAX were performed to properly model the optical response of the LS-DAC in reflectance mode.

2.2.1 Monte-Carlo simulations

FRED software (Photon Engineering, Tucson, AZ) was used for the Monte-Carlo simulations, as described previously[5]. The software utilizes a Henyey-Greenstein approximation of Mie scattering theory and does not take into consideration diffraction, absorption, polarization, or beam steering events introduced by the heterogeneities inherent to real tissue. However, these simulations have been shown to provide an excellent first-order approximation of confocal microscope performance in homogeneous scattering media[5, 38].

Previously, scattering models in reflectance mode for dual-axis confocal (DAC) as well as single-axis confocal (SAC) systems were compared in both line-scanned and point-scanned configurations using Monte-Carlo simulation[5] (**Fig. 2.2.1.1**). The Monte-Carlo scattering simulations are performed without taking diffraction into consideration, based on a Henyey-Greenstein approximation of Mie scattering theory using FRED software. The Henyey-Greenstein function approximates the angular distribution of scattered photons in biological tissues as a function of the sample anisotropy factor (g), and scattering angle (ψ) defined as:

$$p(g,\psi) = \frac{1}{4\pi}\frac{1-g^2}{(1+g^2-2g\cos\psi)^{\frac{3}{2}}} \qquad (16)$$

By setting up the optical components in FRED at their appropriate geometric locations as shown in **Fig. 2.2.1.1** and the scattering response can be simulated for each imaging depth (d) for each anisotropy factor (g). The input parameter for the effective NA of the DAC configuration is 0.17, and the resolution-matched SAC configuration has an NA of 0.42. The results are analyzed and presented in terms of peak signal-to-background ratio as a function of optical length, a dimensionless quantity describing the total mean-free-paths traveled round-trip by non-scattered (ballistic) photons between the tissue surface and the focal plane. The "peak signal" is recorded when a mirror is positioned at the focus. The "background" signal is recorded by removing the mirror from the simulation.

Results show that the PS-DAC has the best imaging performance while the LS-SAC has the worst imaging performance (**Fig. 2.2.1.2a**). At shallow depths (optical length <= 4.5, or <~100 μm equivalent imaging depth), LS-DAC and PS-SAC have similar performance (**Fig. 2.2.1.2b**). Both LS-DAC and PS-DAC show superior contrast in comparison to LS-SAC and PS-SAC, respectively.

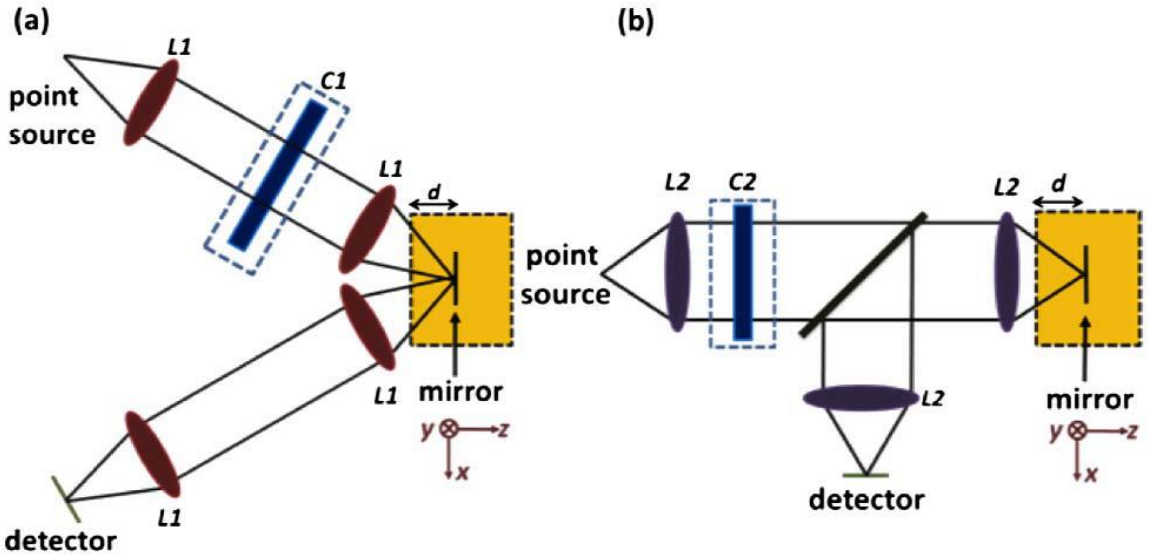

Figure 2.2.1.1. a) DAC microscope setup and b) SAC microscope setup used in the Monte-Carlo simulations[5].

Note: C1 and C2 are cylindrical lenses used only in the line-scanned (LS) configurations.

To put the configurations in perspective, the SAC configuration (PS-SAC in particular) is a generalization of the commercially available confocal microscopes, and the DAC configuration is the prototype being developed in our lab.

The goal for the LS-DAC is to have similar level of imaging contrast as the PS-DAC, at

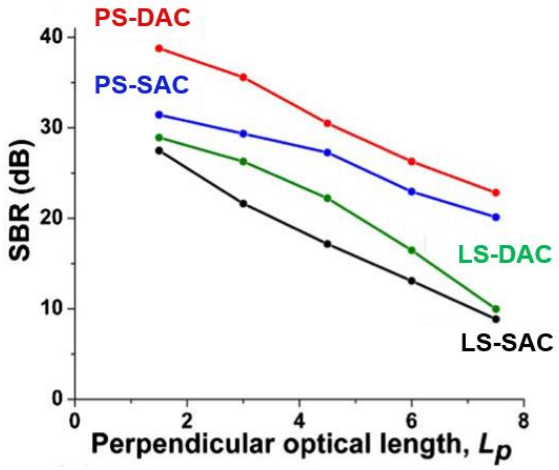

Figure 2.2.1.2. Monte Carlo simulations of SAC and DAC signal-to-background ratio in PS and LS configurations over a range of depths. (L_p is the perpendicular optical length, define as a function of the scattering coefficient μ_s and the imaging depth d, $L_p = 2\ \mu_s d$). Adapted from published work[5]

least at the shallow depths. In other words, the LS-DAC is expected to improve imaging speed

while maintaining an imaging contrast that is generally accepted in commercially available systems.

The contrast for both LS-SAC and LS-DAC is lower than that of the corresponding PS-configurations due to a loss of confocality along one axis that potentially introduces crosstalk between pixels along the imaging line (**Fig. 2.2.1.2**). These results suggest that the LS-DAC could potentially provide the optimal balance between imaging quality and speed–a critical balance for an imaging system that can be translated to the clinic.

Figure 2.2.1.3. Monte Carlo simulations of DAC and SAC in LS and PS configurations[5]

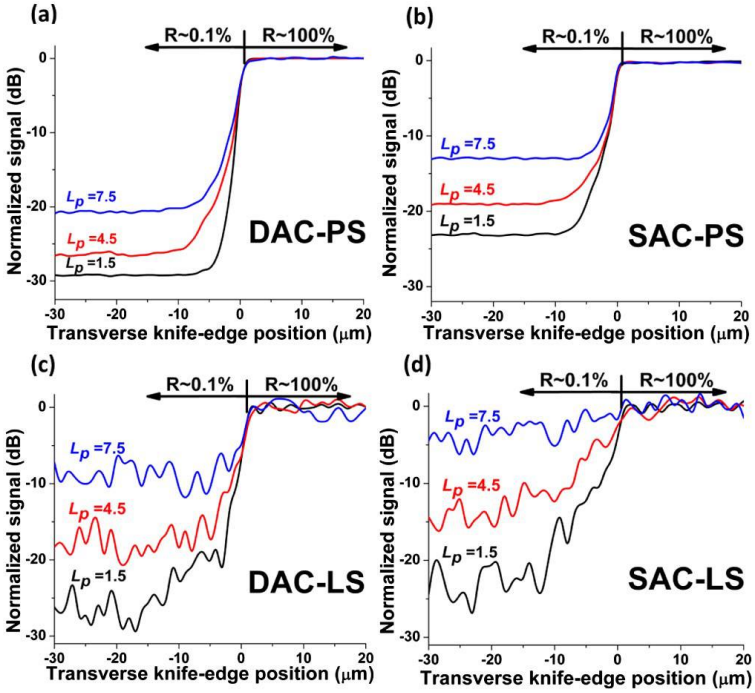

Note: Transverse (lateral) responses of the DAC and SAC to a 30-dB knife-edge show crosstalk levels in LS and PS configurations.

In comparison to panels **(a)** and **(b)**, **(c)** and **(d)** show significant blurring of the knife edge possibly due to crosstalk between pixels.

2.2.2 ZEMAX Raytracing

For diffraction-based system modeling, optical raytracing was performed in ZEMAX (Redmond, WA). The illumination and collection paths were modeled separately.

Illumination side: A 660nm diode laser coupled through a single-mode optical fiber is used as the illumination source. This Gaussian point-source is collimated using a microscope objective lens (L1) with a focal length of 20mm. A weak cylindrical lens (C1, f = -50 mm) is inserted into the collimated portion of the beam path before the light is focused into the tissue by an identical objective lens as L1. This introduces astigmatism into the illumination path, causing the focal planes in the x and y dimensions to be offset, resulting in two orthogonal focal lines. Only one focal line is used for the line-scanned confocal imaging process (**Fig. 2.2.2.1a**). For our particular configuration, we chose to use a negative (diverging) cylindrical lens (OptoSigma Corp, Santa Ana, CA). (Note: ZEMAX raytracing models show no significant difference between using positive and negative cylindrical lenses as long as all the elements in the optical path are properly aligned.)

Figure 2.2.2.1. Illumination arm of the LS-DAC

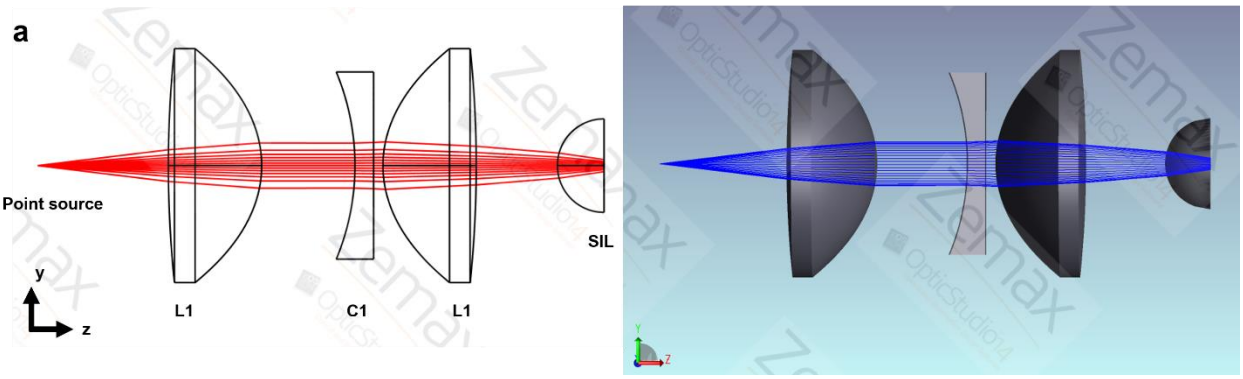

2.2.2.1a. ZEMAX ray-trace setup of the illumination arm of the LS-DAC.

The ZEMAX ray-trace (**Fig. 2.2.2.1b**) shows the line imaged onto the tissue, where the spread (line width) in the ray-traced spots at the focal plane (**Fig. 2.2.2.1c**) is well-within the Airy disk. The Airy disk indicates the diffraction-limited spot size for uniform illumination and allows us to assess the diffraction-limited performance of an optical system. In general, a diffraction-limited system should result in ray-traced beams all focusing to a region within the Airy disk.

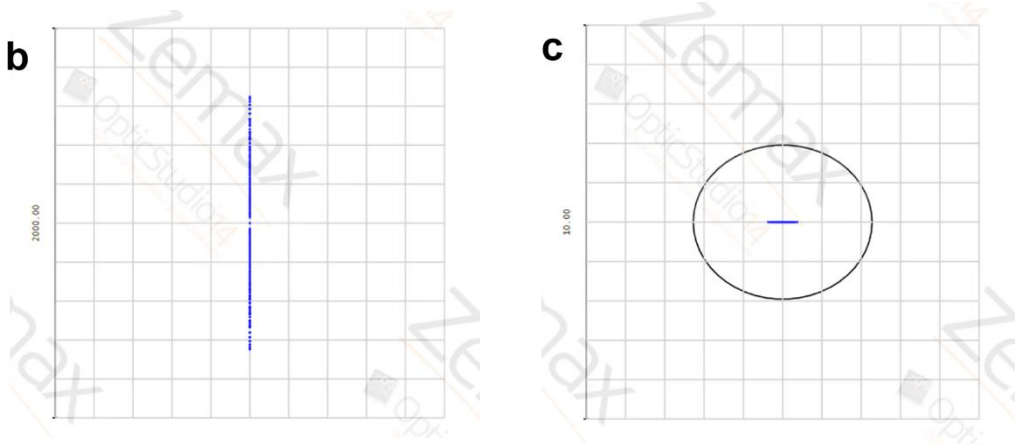

2.2.2.1b. ZEMAX ray-trace spot diagram of the line imaged into the tissue. Grid spacing 200 µm. **2.2.2.1c.** Zoomed-in view of **2.1.1b** at the central pixel of the line. Grid spacing 1 µm. (Note, the spread of the ray-traced spots at the focal plane is within the diffraction-limited spot size indicated by the circle.)

Collection side: The same collimating objective lens (L1) is used to collimate the line image collected from the sample. A focusing lens (L2) with a focal length of 100mm (OptoSigma Corp) provides a 5x magnification for the line imaged into the tissue. The magnified line is imaged onto a sCMOS camera (Hamamatsu Orca Flash 4.0 v2, Hamamatsu Photonics, K.K. Japan) and processed by a custom-developed frame-grabbing software (LabVIEW, National Instruments). A digital confocal slit is applied before the confocal line is processed by the frame-grabber. The ZEMAX ray-trace (**Fig 2.2.2.2**) shows how the line at the tissue is mapped onto the sCMOS camera. A 1-mm line at the tissue corresponds to a ~7.5 mm line at the detector, taking into consideration of the SIL magnification. The sCMOS has a pixel spacing of 6.5 µm.

Figure 2.2.2.2. Collection arm of the LS-DAC

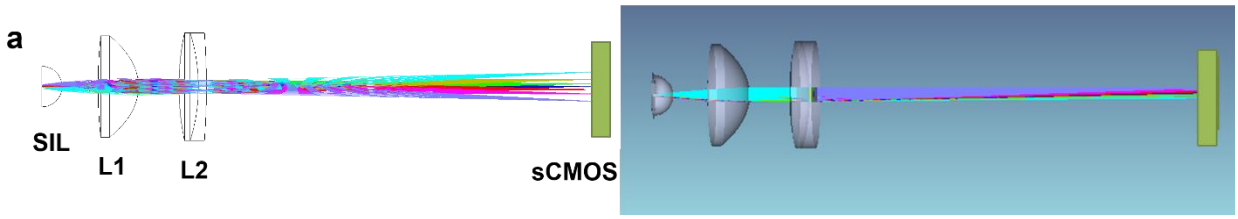

2.2.2.2a. ZEMAX ray-trace of the collection arm of the LS-DAC.

The focal line is treated as a line of point sources in the collection arm located ± 0.5 mm along the y-axis from the optical axis. Optical responses of the system from light source at different points are shown in **Fig. 2.2.2.2b**.

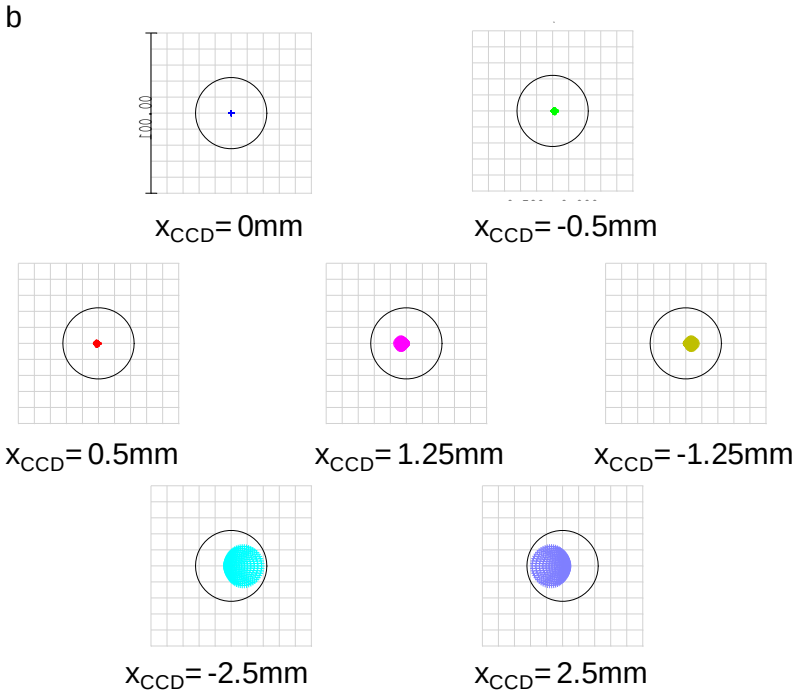

2.2.2.2b. ZEMAX ray-trace of line imaged onto the detector at different locations. Note: the line from the tissue is modeled as a line of point-sources at different locations spanning the 5-mm long line. The spread of the ray-traced spots on the detector is well-within the diffraction-limited spot size.

The results of ZEMAX ray-tracing indicate that the LS-DAC design is diffraction-limited as expected from theoretical calculations. The overall configuration schematic of the LS-DAC is as depicted below:

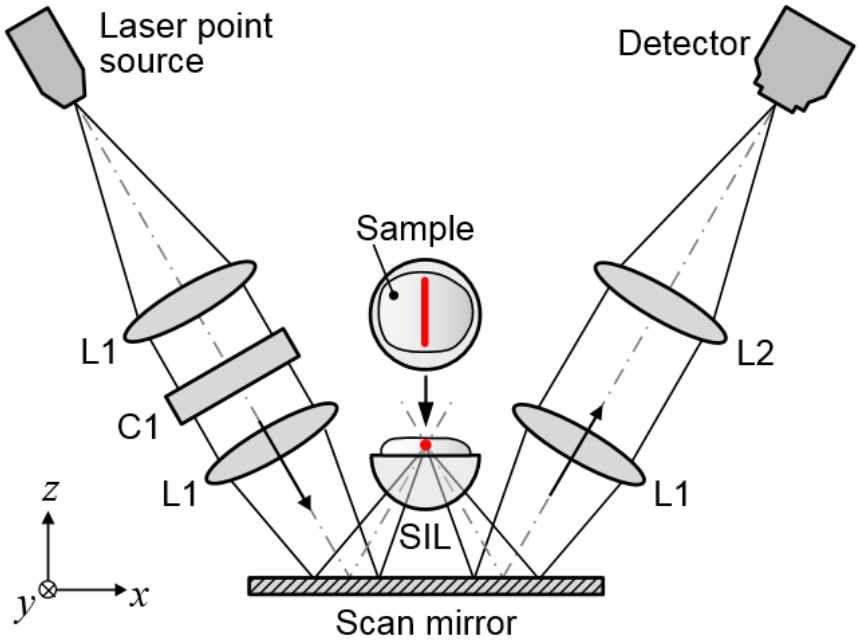

Figure 2.2.2.3 LS-DAC setup schematic

The scanning mirror shown in the **figure 2.2.2.3** is kept stationary for the initial alignment and line-imaging modifications. The mirror reflects the illumination light upwards toward the solid immersion lens (SIL) and into the sample. After the initial alignment and optimization, the mirror will rotate along the y-axis to scan the imaging line along the x-axis within the sample of interest.

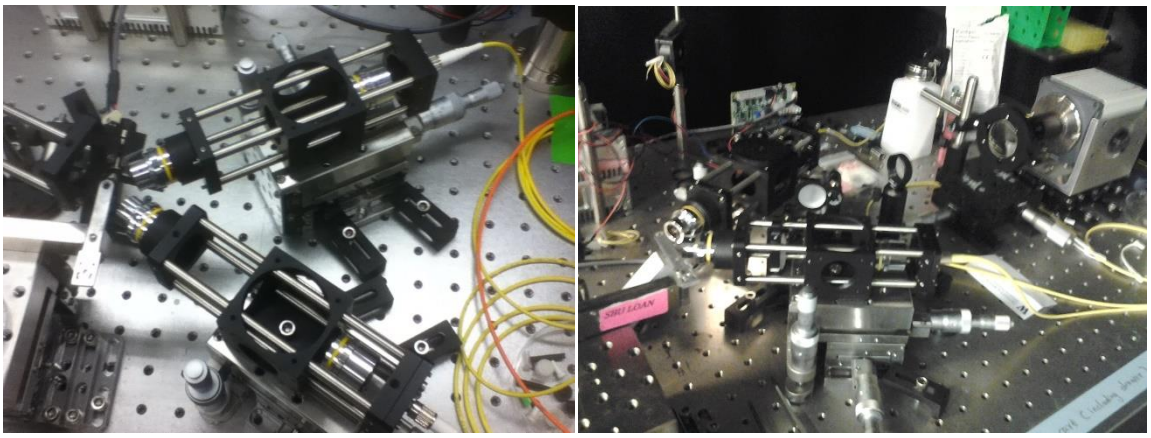

Figure 2.2.2.4. Photograph of benchtop PS-DAC (left) and LS-DAC (right) setup

2.3 System specifications

From calculations and software raytracing, we have established that the expected full-width-at-half-maximum (FWHM) line-width at the tissue is ~2.1 μm, and the FWHM line-length at the tissue is ~0.65 mm, of which, only the center 0.5 mm is used for imaging in order to stay within the center of the Gaussian profile where the intensity is >>50% of the peak intensity. As a

result of the 5x magnification, the expected width of the line at the detector is 2 pixels (at 6.5µm pixel width) and the expected length of the line at the detector is ~500 pixels. Since the minimum line-width allowed for acquiring a region of interest by the camera is 8 pixels, the "confocal-slit" at the detector side will be acquired as an 8x500 pixel strip, further cropped in software down to an appropriate line width (2 - 3 pixels), and then binned into a 1x500 pixel strips. The confocal images are created by stitching the binned strips using a custom MATLAB script (Mathworks). Based on the results from the Monte-Carlo simulations, we expect the LS-DAC to have similar imaging contrast at shallow depths with PS-DAC.

Chapter 3. Characterization of the LS-DAC and comparison with PS-DAC

A LS-DAC system has been designed and built as specified in Chapter 2. Experimental characterizations have been performed to confirm the axial and transverse resolution of the system. In addition, we want to compare the performance of the LS-DAC to PS-DAC to confirm that the imaging capability is comparable at shallow imaging depths.

The system is characterized by measuring the axial and transverse response to a reflective target in water. The comparison experiments for LS-DAC and PS-DAC are performed using a homogeneous liquid phantom (Intralipid) as well as in fresh excised tissue specimens. The imaging performance of the LS-DAC is as expected per design parameters.

3.1 System testing

For the axial response, a highly reflective mirror target is translated along the z-axis through the focus of the microscope (**Fig. 3.1.1**). The system output is collected by the sCMOS camera and plotted as a function of mirror displacement with respect to the focus (z=0). The axial resolution, or the thickness of optical section, is defined as the full-width-at-half-maximum (FWHM) of the axial response plot.

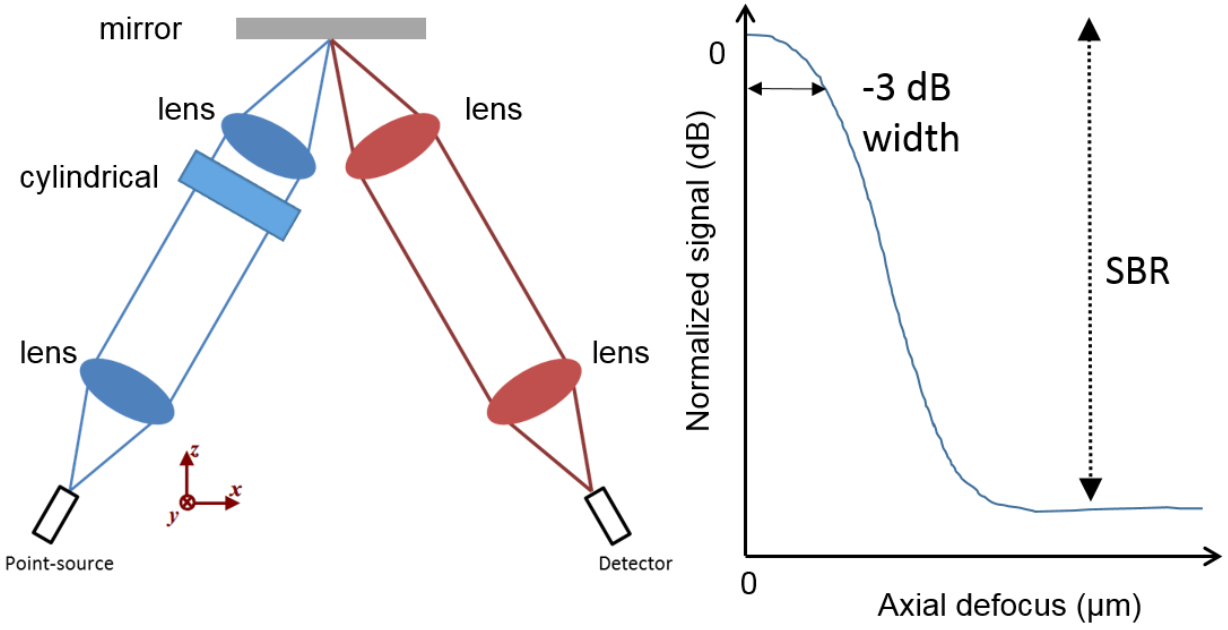

Figure 3.1.1. Schematic of the experimental measurement of axial response

For the transverse response, a knife-edge target consisting of half highly-reflective mirror and half uncoated glass surface is used. The transverse response is be tested separately along the axis parallel (y) and perpendicular (x) to the focal line. When the knife-edge is placed parallel to the focal line, it is translated through the focus along the x-axis. The system output is captured and

plotted as a function of the knife-edge position. The transverse resolution is defined as the distance between the 90% and 10% intensity points during the transition. This is to confirm that the transverse resolution along the x-axis is still comparable to that of the PS-DAC. When the knife-edge is placed perpendicular to the focal line, it will remain stationary at the focal plane (**Fig. 3.1.2**). The line is imaged directly by the sCMOS camera. This transverse response of the LS-DAC system will help us gain a better understand of the extent of pixel crosstalk due to loss of confocality along the y-axis.

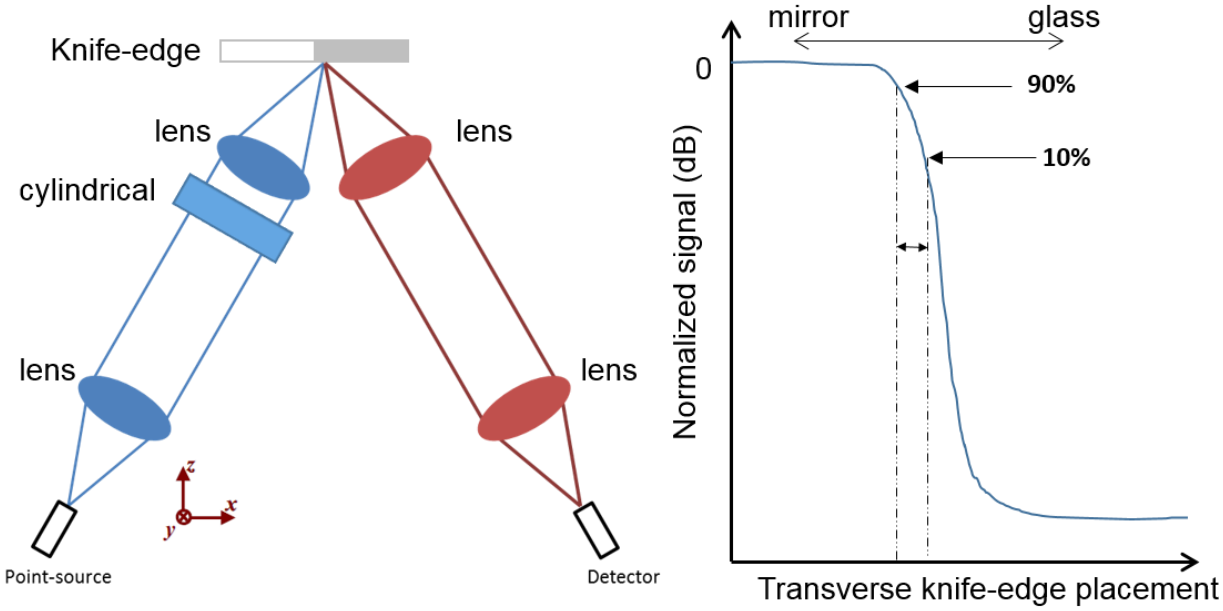

Figure 3.1.2. Schematic of the experimental measurement of the transverse response

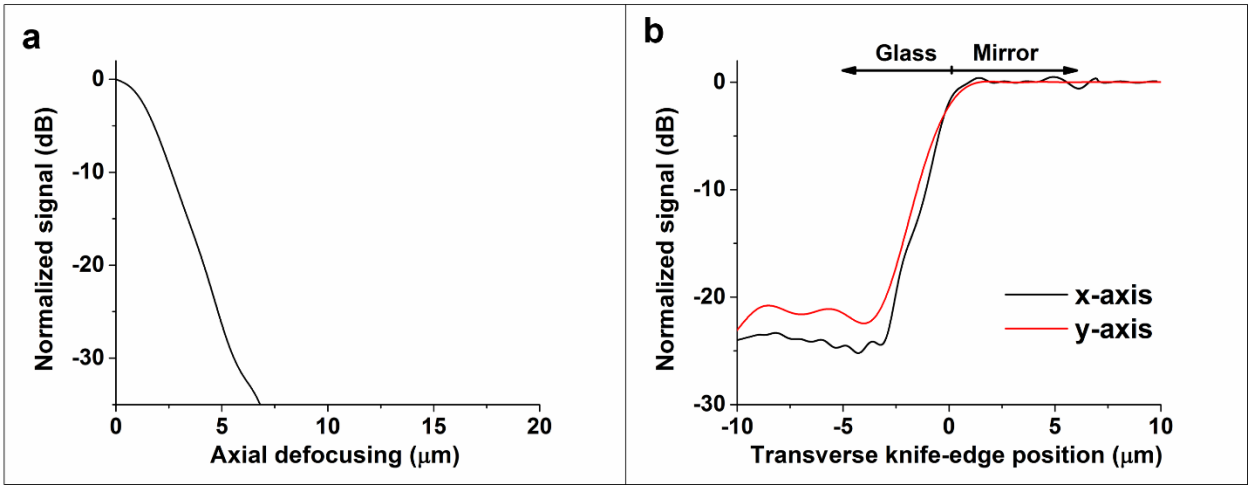

Figure 3.1.3 Experimental characterization of the LS-DAC a) axial response, and b) transverse responses along x- and y-axis.

The experimental results closely match that of the theoretical calculations and software modeling (**Fig 3.1.3**). The axial resolution is ~2.1 μm, and the transverse resolution orthogonal to

the confocal line is ~1.2 µm. The knife-edge response along the line shows a transition width of ~1.3 µm indicating that the pixel crosstalk is not significant.

3.2 Comparison of PS-DAC to LS-DAC

To compare the PS-DAC to the LS-DAC, the cylindrical lens (C1) shown in **Fig 2.2.2.3** can be removed from the illumination arm to return the system to the PS-DAC configuration. This enables us to directly compare the performance of the two configurations with minimal change in optical elements in the system. Note, each time the cylindrical lens is removed or inserted, alignment of the system must be reconfirmed. No significant shift in alignment is expected, but movement in either illumination or collection path of the DAC setup can potentially ruin the alignment and lead to suboptimal imaging condition.

The performance of the PS-DAC and LS-DAC configurations were assessed based on two key parameters: spatial resolution and contrast (signal-to-background ratio, or SBR), as was done in the Monte-Carlo simulations described in Chapter 2. A homogeneous scattering phantom (5% Intralipid) was used to characterize the axial and transverse responses of both configurations. All analyses were performed over a range of optical lengths (OL), a dimensionless parameter defined as $2\mu_s d/\cos\theta$ where d is the physical imaging depth within the sample, μ_s is the scattering coefficient of the sample, and θ is the half angle of intersection (30°) between the illumination and collection beams. The OL is the average number of scattering mean-free-paths ($1/\mu_s$) traversed by ballistic photons during a round trip path to the focal volume and back out of the tissue.

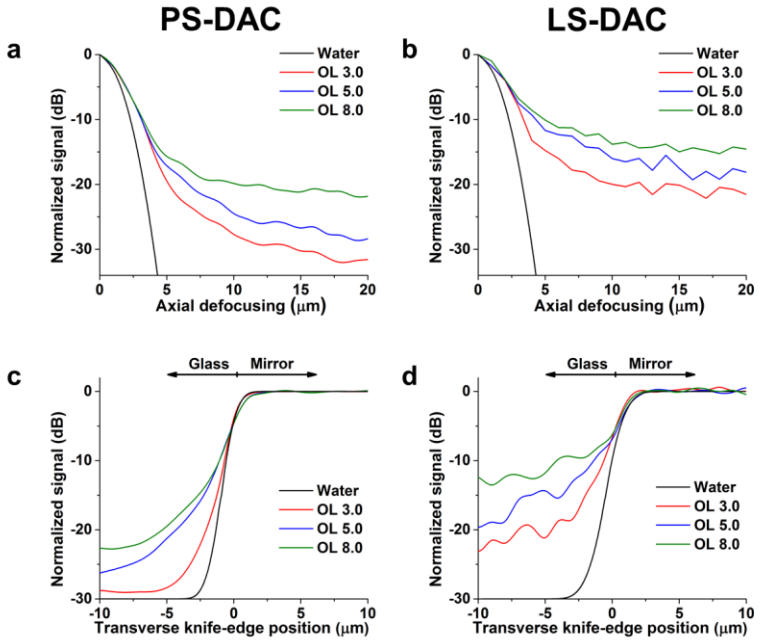

Figure 3.2.1[2]. Results from Monte-Carlo simulations of a homogeneous scattering medium over a range of optical lengths (OL).

(a) The axial response of the PS-DAC microscope. (b) Axial response of the LS-DAC microscope. (c) Transverse response of the PS-DAC microscope. (d) Transverse response of the LS-DAC microscope. Note: the calculated diffraction-limited response in water is plotted as reference.

The axial and knife-edge responses were measured as described previously. A sCMOS camera was used as a detector for reflectance-based measurements of axial and transverse response for both the PS-DAC and LS-DAC microscopes. For the PS-DAC, the detector "pinhole" was selected by binning the center 3x3 pixels at the focus. This corresponds to an actual pinhole size of ~20x20 µm, which is slightly larger than the $1/e^2$ spot size of the imaged spot at the detector.

For the LS-DAC configuration, the imaging slit was defined by a 3x500 pixel region-of-interest on the camera. However, in order to match the conditions of our Monte-Carlo simulations, only a 3x3 bin of pixels at the center of the focal line, corresponding to one resolvable point at the center of the line, was used to construct an axial response plot. Contrast was characterized by the signal-to-background ratio (SBR), which is defined as the ratio between the peak signal when the reflective surface is in focus, and the background signal obtained when the reflective surface is removed from the Intralipid phantom.

Results from Monte-Carlo simulations (**Fig 3.2.1**) comparing the PS-DAC and LS-DAC configurations show that the contrast is lower for the LS-DAC configuration when compared with the PS-DAC.

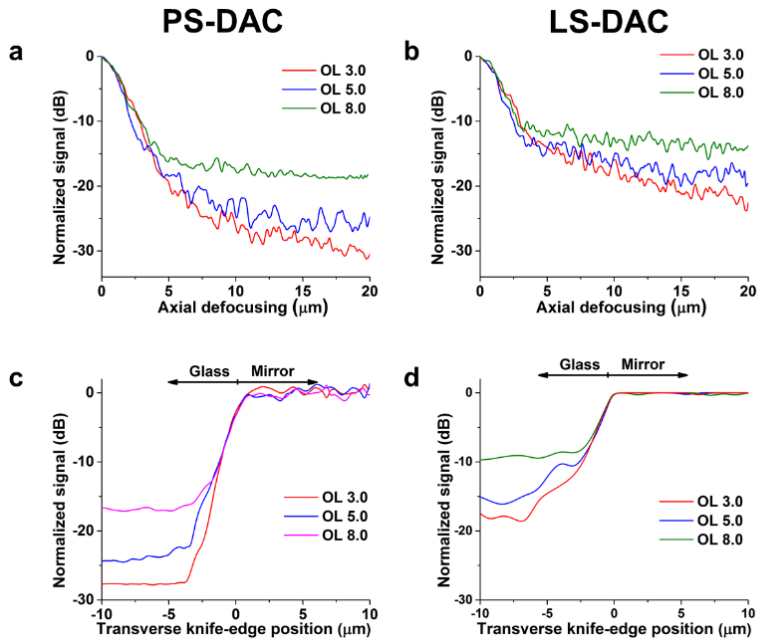

Figure 3.2.2[2]. Experimental characterization of axial and transverse responses over a range of optical lengths (OL) in Intralipid.

(a) Axial response of the PS-DAC microscope. (b) Axial response of the LS-DAC microscope. (c) Transverse response of the PS-DAC microscope. (d) Transverse response of the LS-DAC microscope.

Experiments with a homogeneous scattering medium, i.e. Intralipid (**Fig. 3.2.2**), indicate that the axial and transverse resolutions are similar for both the line-scanned and point-scanned configurations. At shallow depth, the line-scanned and point-scanned DAC microscopes show comparable spatial resolution (2.2-μm axial, 1.3-μm lateral) and image contrast. In both cases, the background is higher (contrast is lower) for the line-scanned configuration due to the loss of confocality along one dimension. The experimental performance of both configurations matches the results from their corresponding Monte-Carlo simulations.

The LS-DAC system performs as expected per calculation and simulations for both non-scattering and scattering samples. A proof-of-principle is performed to demonstrate the imaging capability of the system in fresh biological tissue.

The comparison imaging experiments were done in fluorescence mode. A long-pass fluorescence filter (Chroma, PN: 421799) was placed in the collimated region of the collection path to block the reflected illuminating laser light. Alexa Fluor 647-conjugated dextran (AF647-dextran 10kDa, Invitrogen) was injected retro-orbitally into anesthetized mice (Ketamine/Xylazine, 100 mg/kg body mass) to highlight the brain vasculature. The mice were

immediately sacrificed and the whole brains were then excised for imaging of the superficial vasculature (up to 200-µm deep).

Different detectors were used for the PS-DAC and the LS-DAC setup. In the PS-DAC setup, fluorescence signals were coupled into a photomultiplier tube (PMT, H7422-40, Hamamatsu) using a single-mode fiber. A galvo scanning-mirror was driven at its resonance frequency to scan the focal spot along the y-axis in the sample. A computer-controlled micrometer is used to scan the sample stage along the x-axis in 1-µm steps, and a piezoelectric actuator is used to scan through 450 µm in depth at 2Hz. Pixel intensities captured during the raster-scanning of the focal spot are mapped and rendered with a custom LabVIEW (National Instruments) frame-grabber program as detailed previously[35]. The 3D volumes from imaging the tissue are constructed by a series of vertical slices.

In the LS-DAC setup, the sCMOS camera is used to capture the focal line at 1-ms camera exposure. The galvo mirror is kept at its neutral position and a computer-controlled micrometer is used to scan the sample stage along the x-axis in 1-µm steps. The piezoelectric actuator is not used for depth imaging; instead, the imaging depth is manually adjusted by a micrometer in the z-axis

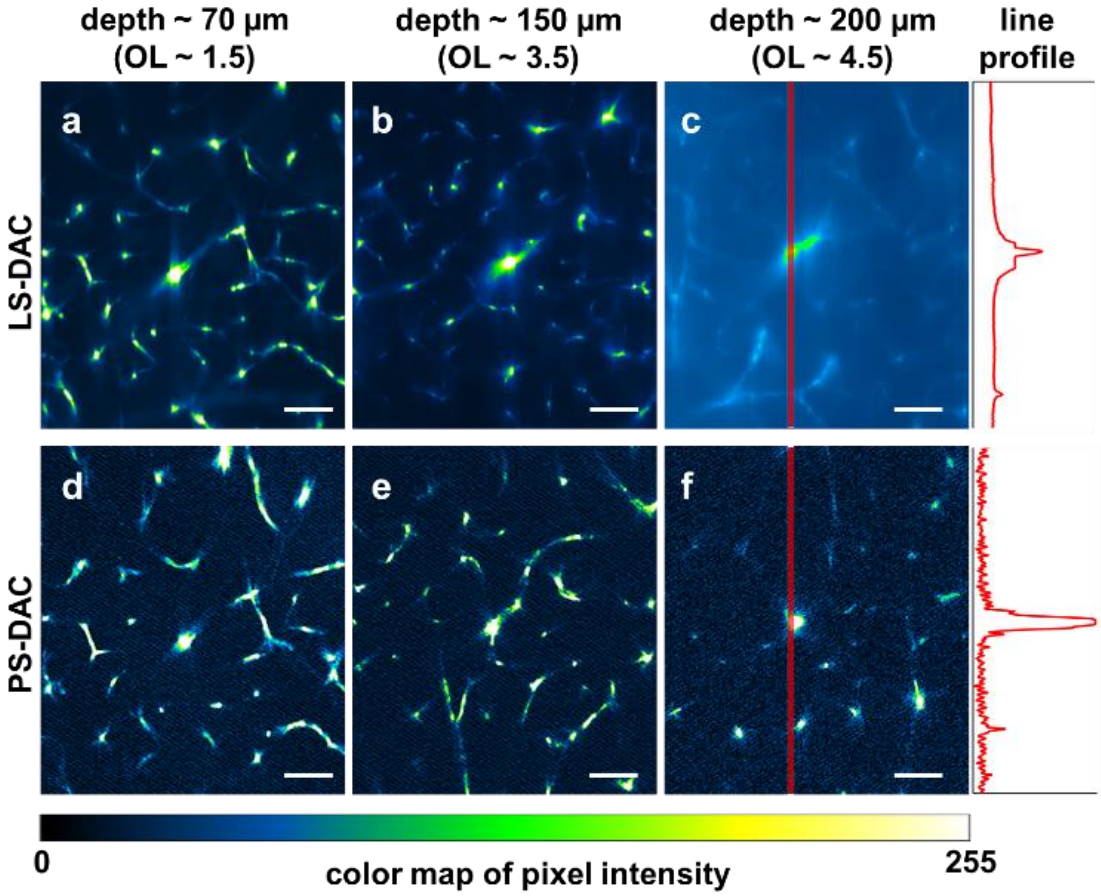

Figure 3.2.3[2]. Comparison of LS-DAC (a-c) and PS-DAC (d-f) performance via fluorescence imaging of identical mouse brain vasculature at depths of up to 200 µm. The intensities of the pixels along the red band in (c) and (f) are plotted on the right. Scale bar = 70 µm.

on the translational stage. The captured frames of the scanned focal line are rendered into individual *en face* images using a custom MATLAB (MathWorks) script.

A side-by-side comparison of PS- and LS-DAC is presented (**Fig. 3.2.3**).The OL corresponding to each imaging depth is estimated based on a previously reported value of the scattering coefficient for brain tissue, $\mu_s \sim 10\ mm^{-1}$ [39]. The background in the line-scanned system starts to overwhelm the signal when imaging at depths of around 150 µm, degrading the contrast of the image. In addition, beyond a depth of 200 µm, a slight degradation in lateral resolution is also seen in the LS-DAC images while this is not seen in the PS-DAC images.

3.3 Conclusion and limitations

The structural details of the brain vasculature can be visualized clearly in both PS-DAC and LS-DAC setups. The SBR of the PS-DAC is higher than that of LS-DAC, yet the PS-DAC images appear grainy whereas the LS-DAC images appear smooth. This is likely due to the short pixel dwell time of a PS-DAC system, which often results in a lower signal-to-noise ratio (SNR) that can deteriorate the image contrast. While the background is overwhelming the signal at 200 µm imaging depth for the LS-DAC, the highlighted vasculature can still be discerned visually.

Under photon-starved imaging conditions as is often the case with fluorescence microscopy, image contrast may be limited by shot noise and detector noise rather than the background noise from out-of-focus fluorescence. Therefore, under low-signal conditions (e.g., weak fluorescence), with a high-sensitivity camera, the performance of a LS-DAC microscope is potentially superior to a PS-DAC microscope at shallow depths.

At matching frame-rate of 2Hz, the ability of the LS-DAC to obtain images with high resolution and high contrast is limited to superficial depths of < 200 µm whereas PS-DAC is able to image at 250 µm or more in depth. The optimal imaging depth of the LS-DAC system in fluorescence mode at 1-ms camera exposure is limited to < 150 µm.

Chapter 4. A Heterogeneous Phantom

4.1 Background and motivation

When comparing the LS-DAC to PS-DAC performance previously, 5% Intralipid was used as a homogeneous scattering phantom. Intralipid is a commercially available homogeneous lipid emulsion used as a reproducible scattering phantom for many biophotonics applications[34, 40]; however, it was found that Intralipid does not accurately model the resolution degradation due to the presence of heterogeneities observed in real tissue (**Fig. 4.1.1**).

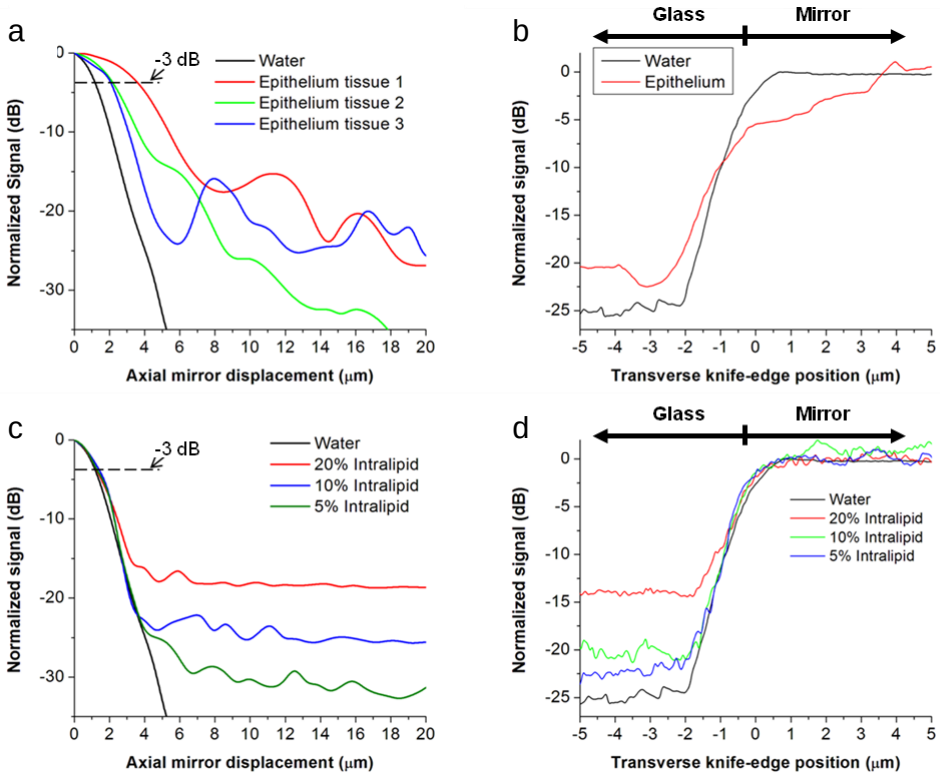

Figure 4.1.1. Axial and transverse responses of the tabletop PS-DAC for heterogeneous (a, b) and homogeneous samples(c, d)[4] showing degradation of axial and transverse resolution in heterogeneous samples, but not in homogeneous samples.

For all device developments, having a standardized or at least a highly reproducible method for verifying and validating the design is critical. Ideally, one method would be used for all relevant device testing in the field (optical imaging in our case). However, such general designs would be unrealistic if one desires to characterize every imaging device in a thorough manner. As a result, various different optical phantoms have been developed for specific imaging modalities and specific imaging targets. For example, phantoms mimicking optical, mechanical, as well as structural properties of tissue[41] have been developed for use with popular optical imaging techniques such as optical coherence tomography[42, 43], spectral imaging[44] and conventional reflectance confocal microscopy[45]. Similarly, in this study, we have designed an optical-

scattering phantom to verify the performance of a reflectance-based dual-axis confocal (DAC) microscope for imaging unprocessed fresh human skin.

Due to the design of the DAC system, the illumination and collection beams can be misaligned due to heterogeneity-induced refractive beam steering and lensing effects. Therefore, a heterogeneous scattering phantom is developed to help us understand the extent to which the heterogeneities affect the system's imaging quality.

To keep the testing conditions constant throughout the design, the phantom testing was performed in the PS-DAC configuration. A piece of fresh full-thickness human epithelium was secured on the surface of the mirror used to perform the axial and transverse scans to obtain the traces in **Figure 4.1.1** panels (a) and (b). Note: the imaging resolutions degraded in both cases. The axial and transverse responses of the PS-DAC to homogeneous samples, both non-scattering and scattering (water and Intralipid), are shown in panels (c) and (d). Note: no resolution degradation is observed.

4.2 Design rationale

The phantom is designed using a "black-box approach" where when input A passes through the black-box yields output B. In this case, A is the laser illumination, the epithelial tissue is the black-box and the corresponding output is B. Since the epithelial tissue is heterogeneous and varies greatly from patient to patient and within patients, there are few generalizations that can be made. The goal for this design is to select a sample composition that mimics the black-box closely and consistently. The following parameters were considered.

A. Choice of material

Rough design parameters are established by elementary knowledge of human skin samples. We know that the average cell size in the epithelium ranges from ~10 - 70 μm in diameter. Similar to the rest of the human body, the epithelial tissue is expected to have an aqueous component. So our starting point for the design is to have an aqueous mixture with spheroid heterogeneities sized in the range of 10’s of microns.

We know that in addition to beam steering properties, the skin contains a highly scattering component, similar to most biological tissues. Since objects sized on the order of microns are too large to mimic the Mie scattering observed in biological tissues, a scattering medium needs to be added in addition to mixture. In this case, we chose Intralipid, an established optical phantom component used in homogeneous phantoms. Note, Intralipid was used alone as a scattering phantom and would be sufficient in most systems when beam steering is not a significant issue. Due to the general non-overlapping property of the illumination and collection arms of the DAC setup, any heterogeneity in either beam path has the potential of distorting the beam path and degrading the resolution along with the contrast of the images obtained by the system.

To generalize, the aqueous phantom mixture will have the heterogeneous spheroids to mimic beam steering, Intralipid component to mimic scattering, and sufficient water or saline to ensure the final concentration of different components roughly corresponds to the density of different light distorting components in real tissue.

At first, it was suspected that the actual material makeup of the beads would create different beam steering properties, but after rough testing of various sizes of Silica beads (U.S. Silica, Berkeley Springs, WV), it was evident that there is an optimal heterogeneity size for beam steering (**Fig 4.2.1**).

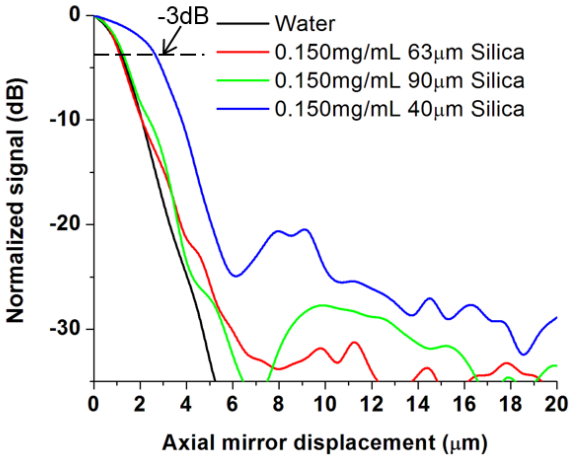

Figure 4.2.1. The PS-DAC's axial response to aqueous mixtures of identical concentrations of silica beads of various sizes. 40-μm heterogeneities in an aqueous mixture elicited a notable degradation in the DAC's axial resolution

B. Determining the concentration of different components used

An aqueous sample made up of beads from a single stock at different concentrations are made and the optical properties measured. The samples with the highest concentration exhibit contrast as well as resolution degradation in the knife-edge responses. The reproducibility of the high concentration samples is very low as with the increase of number of particles in the aqueous suspension/mixture, the mixture is stable for a very short amount of time.

The concentration of the Intralipid is also "titrated" in a similar fashion by serial dilution to ensure that the sample creates approximately the same optical response as the actual tissue. This process requires an immense amount of patience and many inevitable confrontations with failure.

C. Stability

Since the phantom is heterogeneous and aqueous by design, one must ensure the components do not separate and settle out of the mixture. Aqueous mixtures with higher viscosity than saline can also be used to increase the stability of the phantom. If the heterogeneities stratify too quickly in an aqueous solution, phantoms in other phases, e.g. gelatinous, can also be designed.

D. Reproducibility

In our experiments, the standard error of the mean is < 20%. This is significantly lower than anything achievable by real tissue. A lower variation is desirable if this optical phantom were to be commercialized for use on other optical setups.

4.3. Phantom testing

We chose to develop a liquid-based phantom since the highly deformable nature of the phantom will ensure consistent contact between all surfaces during the test, which in turn minimizes error or inconsistency that can be introduced by undesired air-gaps. An aqueous suspension of poly-dispersed silica beads (MIN-U-SIL®40, U.S. Silica, Berkeley Springs, WV) had been prepared at relatively low concentrations (0.15 mg/mL starting concentration) to ensure sample temporal stability. These beads have a median diameter of 10.5 μm with a maximum diameter of 40 μm, appropriate for mimicking the size of cellular and subcellular refractive heterogeneities. The suspension concentrations were adjusted by water dilution. In certain samples, 20% Intralipid (Sigma Aldrich) was added as a homogeneous scattering component.

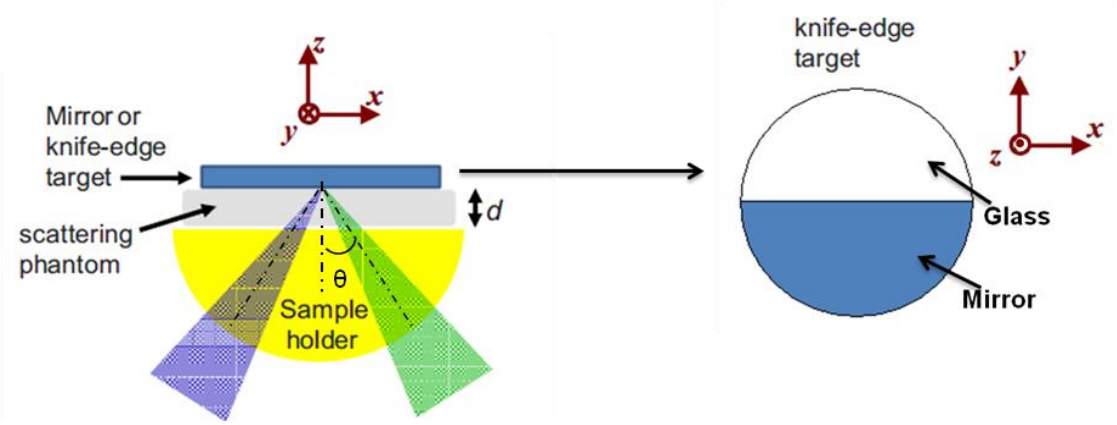

Figure 4.3.1. Schematic of experimental setup with the DAC microscope[4]

The phantom design was evaluated by performing axial and transverse response measurements on our tabletop PS-DAC system. The system response is characterized along the axial as well as the transverse direction as described in previous sections.

In addition, an empirical effective scattering coefficient ($\mu_{s\text{-}eff}$) is defined to quantify the signal degradation as a function of imaging depth due to signal loss from both true-scattering (μ_s) and from lensing/refractive beam steering misalignments. For these measurements, the peak output intensity of the microscope is obtained when the mirror is placed at the focus of the microscope. This peak signal is recorded as the focus of the microscope, and the mirror (always positioned at the focus), are adjusted over a range of shallow imaging depths in each sample. Since the in-focus signal at shallow depths is predominantly due to ballistic (unscattered) photons, the $\mu_{s\text{-}eff}$ can be calculated using the Beer-Lambert relation,

$$\mu_{s-eff} = \frac{1}{L_1 - L_2} \ln\left(\frac{I_2}{I_1}\right)$$

where L_i is the path-length of the ballistic photons through tissue at location i and I_i is the corresponding detected peak signal. For a DAC microscope (**Fig. 4.3.1**), $L_i = 2\, d_i/\cos\theta$, where d_i is the physical depth of the imaging plane at location i. L_i is the total round-trip path-length traversed by ballistic photons through the tissue (and reflected off the mirror) when the illumination and collection axes of a DAC microscope have a crossing half-angle of θ. Here we emphasize again that $\mu_{s\text{-}eff}$ is not a true scattering coefficient, but an empirical constant to describe signal loss as a function of depth due to both true scattering (μ_s) AND refractive misalignments and optical aberrations.

The concentration of silica beads along with Intralipid in the samples are adjusted until the phantom design reproducibly mimics the scattering and heterogeneous refractive properties of unprocessed normal fresh human epithelial samples. The depth dependency of the phantom is characterized at relevant imaging depth of ~75-125 μm, corresponding to the dermal/epidermal junction where the majority of abnormalities are noted at an early stage.

4.4 Results

In all phantom experiments, water samples are used as a non-scattering control to measure the diffraction-limited axial and transverse resolution of the system. It was observed that the resolution degradation is more noticeable along the axial direction, so the initial screening of phantom formulations is performed by measurements of the axial response only. The axial responses were measured using MIN-U-SIL40 suspensions at 0.15 mg/mL, 0.075 mg/mL, and 0.0075 mg/mL initially. These values were chosen arbitrarily to cover a range of concentrations spanning 2 orders of magnitude. Results show that at 0.15 mg/mL and 0.075 mg/mL, the degradation of the axial resolution is still noted. However, when the bead concentration drops to 0.0075 mg/mL, the resolution degradation is no longer observed (**Fig. 4.4.1**).

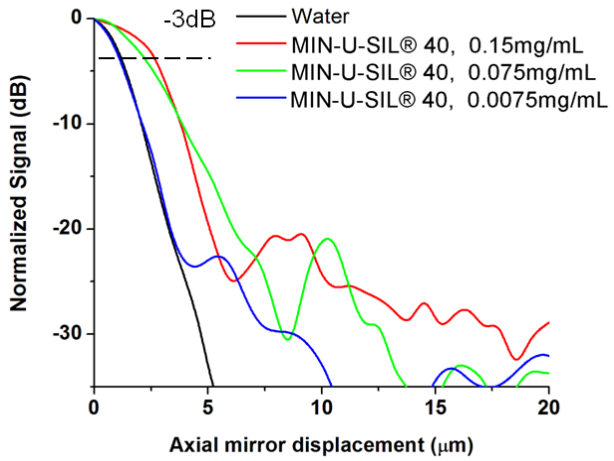

Figure 4.4.1. The axial response of the DAC microscope when investigating different concentrations of MIN-U-SIL40 bead suspensions[4]

In aqueous suspensions with beads alone, there is a direct coupling between $\mu_{s\text{-}eff}$ and the resolution degradation. By decreasing the concentration of beads in solution to the lowest level where the degradation in resolution is still noted, we increase the temporal stability of the sample (stable for >10 minutes). To compensate for the loss of scattering events due to decreased bead concentrations, a low concentration of Intralipid was added, thereby allowing us to tune the true-scattering component of $\mu_{s\text{-}eff}$ independently of the resolution degradation. Representative results of phantom formulations with beads and Intralipid are shown (**Fig. 4.4.2**).

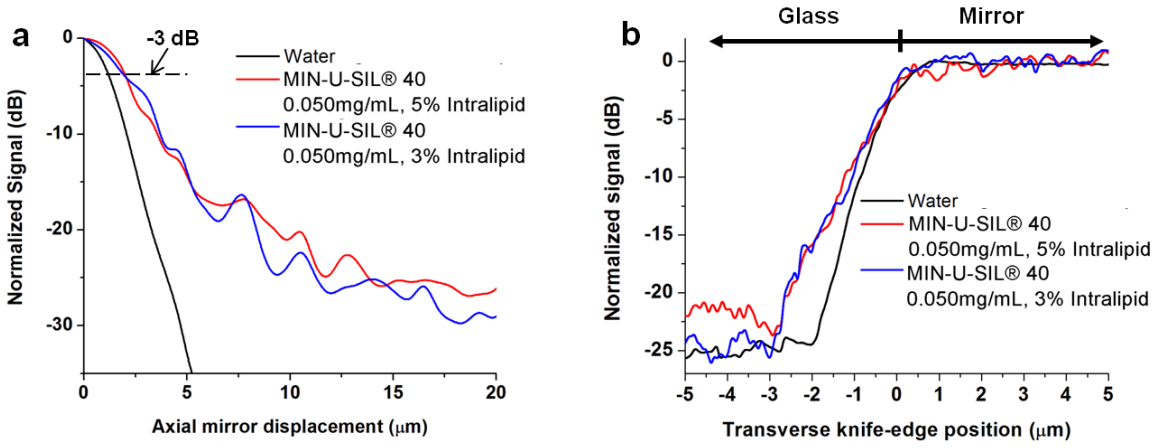

Figure 4.4.2. (a) The axial and (b) transverse response of the DAC microscope when imaging different formulations of tissue phantoms[4].

Table 2 summarizes the results from phantom testing. The phantom formulation of 0.05 mg/mL MIN-U-SIL 40 beads in 5% Intralipid has the highest reproducibility.

Sample	$\mu_{s\text{-}eff}$ (mm^{-1}) ± std. dev.	Axial resolution (μm) ± std. dev.	Transverse resolution (μm) ± std. dev.
Water	NA	2.1 ± 5%	1.2 ± 5%
20% Intralipid	43.9 ± 14% (n=6)	2.1 ± 10%	1.2 ± 10%
10% Intralipid	23.1 ± 14% (n=6)	2.1 ± 10%	1.2 ± 10%
5% Intralipid	12.0 ± 6% (n=6)	2.1 ± 10%	1.2 ± 10%
0.15 mg/mL MIN-U-SIL®40	77.3 (n=1) *note: not stable*	3.1	NA
0.075 mg/mL MIN-U-SIL®40	11.8 ± 18% (n=6)	3.7 ± 26%	NA
0.0075 mg/mL MIN-U-SIL®40	1.9 ± 16% (n=6)	2.2 ± 10%	NA
0.05 mg/mL MIN-U-SIL®40, 3% Intralipid	8.1 ± 16% (n=6)	3.4 ± 16%	2.0 ± 12%
0.05 mg/mL MIN-U-SIL®40, 5% Intralipid	11.0 ± 8% (n=12)	3.4 ± 12%	2.0 ± 8%

Table 2 Summary of phantom testing[4]

Lastly, the depth dependency of the final phantom formulation was tested. The results show that the resolution degradation reaches a relatively constant level at depth above 100 μm (**Fig. 4.3.3**).

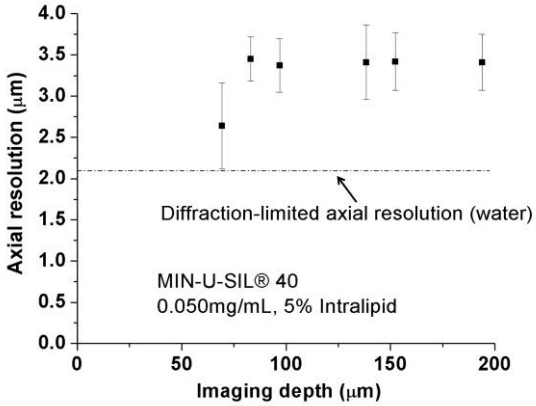

Figure 4.4.3. The axial response of the DAC microscope as a function of imaging depth through a heterogeneous phantom. Error bars correspond to 1 standard deviation from the mean[4].

4.5 Conclusion and limitations

This heterogeneous tissue phantom (**Fig. 4.5.1**) does not mimic the structure of the human epithelial tissue, as it was never our intention to make artificial human skin. Instead, the "black-box" phantom mimics similar responses from the imaging system in a highly reproducible manner. This phantom can potentially be a necessary component for assessing the alignment, sensitivity, resolution and contrast of various prototypes of optical sectioning microscopes under development and in various stages of preclinical and clinical testing. In particular, since our ultimate goal is to translate miniature microscopes into the clinic for *in vivo* image-guided tumor resection and diagnostics[46], it is critical to develop a standardizable testing method and phantom to ensure the consistent performance of devices at multiple testing sites.

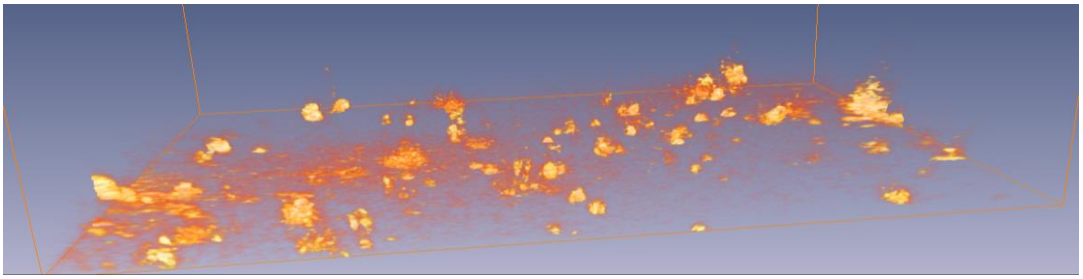

Figure 4.5.1. Sample 3D volume rendering of a phantom sample

Due to the simplicity of this phantom composition, it can be easily made and adjusted to potentially suit different design parameters for other microscopy setups. A heterogeneous phantom as such will potentially be useful for the development of novel imaging approaches in understanding the effects of tissue scattering and beam-steering properties[47-49].

Chapter 5. *Ex vivo* Fluorescence Imaging of Biological Specimens

Imaging of excised specimens is a well-established approach for determining the pathological status of biological tissues, as seen in standard histopathology. *Ex vivo* imaging can be performed in reflectance or fluorescence mode. In this thesis, all of our imaging experiments were performed in fluorescence mode. This chapter provide a general demonstration of the *ex vivo* imaging capability by the LS-DAC.

Fluorescence agents were introduced into the tissue primarily through the animal's circulatory system and topical staining. The acquired LS-DAC images have subcellular resolution and high imaging contrast.

5.1 Excised fresh mouse brain vasculature in fluorescence

Using fluorescence-conjugated dextran to label vasculature has been a well-established way to introduce fluorescence into the biological tissue. This can be done by tail-vein injection in murine, or retro-orbital injection in most animal models. The maximum allowable volume is slightly higher for tail-vein injection compared to retro-orbital injection, thus mistakes made when performing a tail-vein injection is less likely to instantly kill the animal subject. The drawback to tail-vein injection is that the fluorescence is allowed to travel throughout the subject's body, so there is little control of the fluorescence labeling at a specific location of interest. In *ex vivo* imaging experiments, the subjects are immediately sacrificed (within 1 minute post-injection). During the fluorescence imaging of highlighted brain vasculatures, retro-orbital injections are used to introduce the fluorescence-conjugated dextran into the tissue.

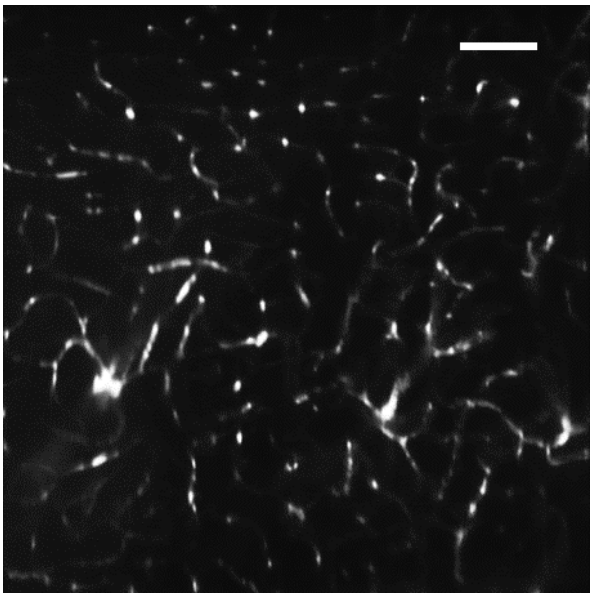

Figure 5.1.1. A typical image of fresh mouse brain vasculature in fluorescence obtained on the LS-DAC at 1ms exposure. Scalebar = 100 μm.

The fresh brain tissue is extracted from the animal upon sacrifice and immediately placed onto the sample stage and imaged without further processing. A typical image obtained from a stage-scanned LS-DAC is shown above (**Fig 5.1.1**).

As time progresses, the fluorescence dye inevitably extravasates into surrounding tissues. While one can still observe strong fluorescence signal, the imaging contrast degrades as photobleaching and extravasation take place. Imaging experiments of a fresh fluorescence sample should be performed within an hour of injection for optimal performance.

5.2 Excised topically stained mouse tissues

Topically staining tissue is another well-established technique often used to non-specifically and superficially stain biological tissue. However, since these imaging studies are used to characterize the performance of the microscope and not the diagnostic a one particular disease, the targeted contrast agents are not used here. Instead, non-specific staining of the tissue is the approach chosen.

Methylene blue (MB) has been used for staining in various medical practices[50-52]. Its fluorescence spectra is similar to that of AlexaFluor 647 dye, which is much more photo-stable and in turn only available in small quantities at a high price. All topical staining in these experiments are done using MB. If the LS-DAC can capture desired details with tissues topically stained with MB, imaging with better fluorescent dyes will only improve the performance.

In order to efficiently stain tissue topically, it is beneficial if the tissue were meant for absorbing surrounding substances *in vivo*; therefore, the tissues along the GI-tract are ideal targets. Some images of the mouse duodenum, kidney, and tongue specimens are presented here.

Duodenum sample prepping:

A segment of intestine directly after the stomach (duodenum) was excised from a sacrificed mouse. The duodenal tissue is rinsed thoroughly with isotonic saline to eliminate any residual food or waste content. One end of the duodenum was tied with a piece of suture, and a solution of stock-concentration MB (1%, Fisher Scientific, S25429) was added through the open end of the duodenum. After filling the duodenum with MB, the open end of the intestine is also tied with a piece of suture. The tissue was allowed to stain for < 15 minutes, then the sutures were cut and the tissue rinsed 4 times for 30 seconds each in isotonic saline. The intestine was then flayed open to expose the stained surface. Confocal images of the stained surface were obtained on the LS-DAC at 1ms camera exposure, with a total imaging time of 0.5 second (**Fig. 5.2.1**). The cellular structures of the duodenal (Brunner's) glands were clearly visible (compare to histopathology), indicated with arrows in both.

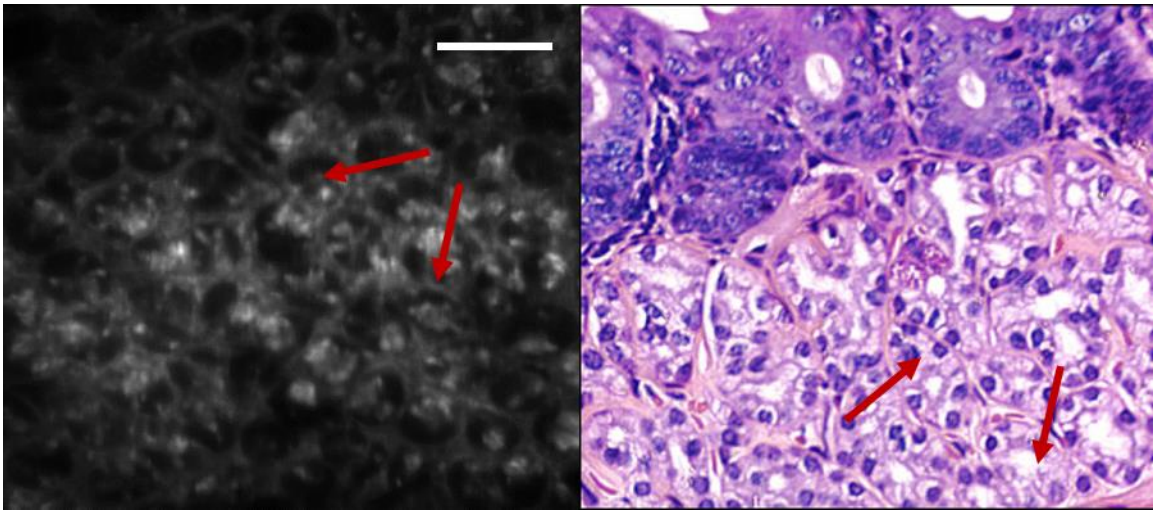

Figure 5.2.1. LS-DAC image of a duodenal tissue stained with methylene blue (left) with a reference H&E stained duodenal tissue from histology (right). Scalebar = 100 µm.

Some images were acquired intraluminally (imaging through the outside of the intestine without flaying the intestine open) out of pure curiosity. As expected, the serosa, outer membrane of the intestine, served as optical deterrent so the imaging contrast was suboptimal. The fact that we were still able to visualize crypt-like structures under these conditions was a pleasant surprise, as the limit of imaging depth of the LS-DAC could be deeper than we expected (**Fig 5.2.2**).

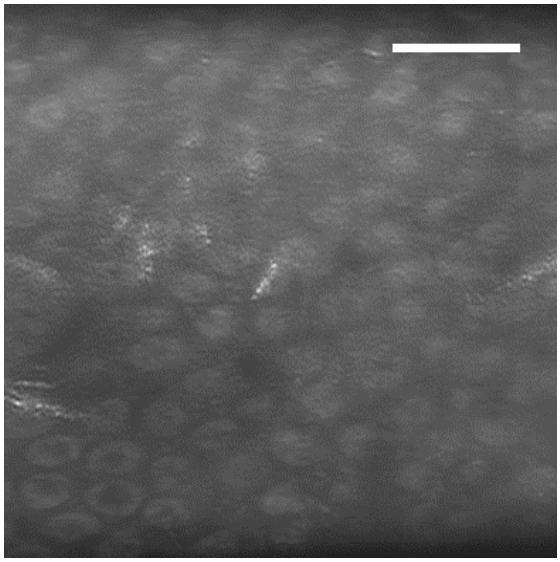

Figure 5.2.2 Intraluminal imaging of duodenal tissue. The ability to visualize crypt-like structures could be due to the thinning of the outer lining of the GI tract as well. Scalebar = 100 µm.

Kidney sample prepping

Unlike with the intestines, internal staining of the kidney was done by cutting open the kidney then topically staining the exposed cut surfaces. The staining was done with the same stock-solution of MB for < 15 minutes then rinsed in the same fashion and imaged immediately. The outlines of (without extensive histological knowledge) renal medulla structures were visualized (**Fig 5.2.3**).

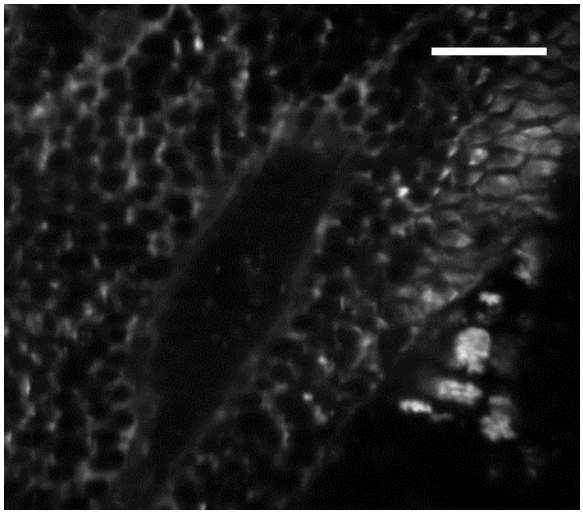

Figure 5.2.3. Topically-stained mouse kidney tissue showing the renal medulla. Scalebar = 100 µm.

Tongue sample prepping

Tongue specimens were of interest because of its similarity in location to oral cancer. Being able to visualize structures in oral tissue is critical in the diagnostic and early detection of dysplastic lesions. The signs of dysplasia typically include the loss of organized cellular structure and enlarged/multiple cell nucleus.

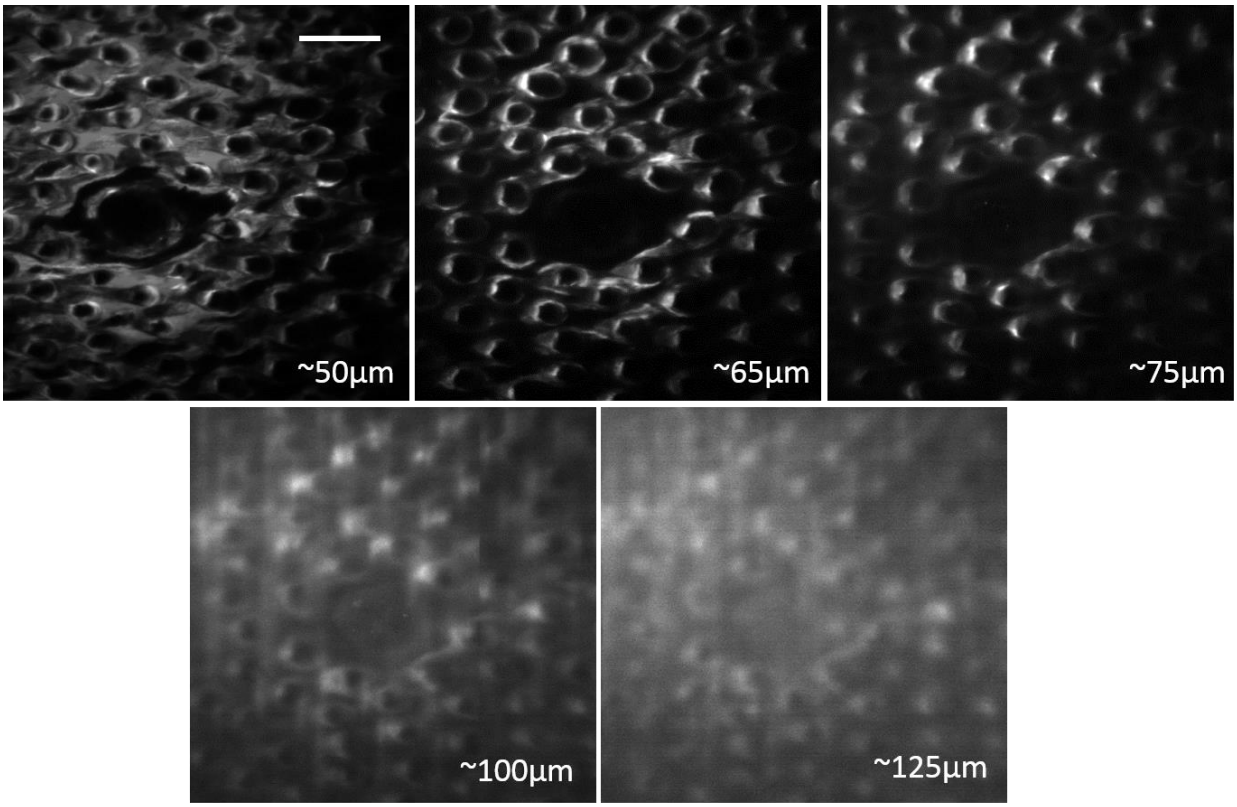

Figure 5.2.4. *En face* images of a topically stained mouse tongue sample at various depths. The contrast has been severely degraded at an imaging depth of ~125 µm. Scalebar = 100 µm.

The tongue specimen was excised and stained topically following the procedures for other MB tissue staining. The images of a normal tongue specimen are presented over superficial depths (**Fig. 5.2.4**). We can see that the contrast degrades significantly beyond 100 μm imaging depth; however, we are still able to visualize the fungiform papillae and its surrounding filliform papillae.

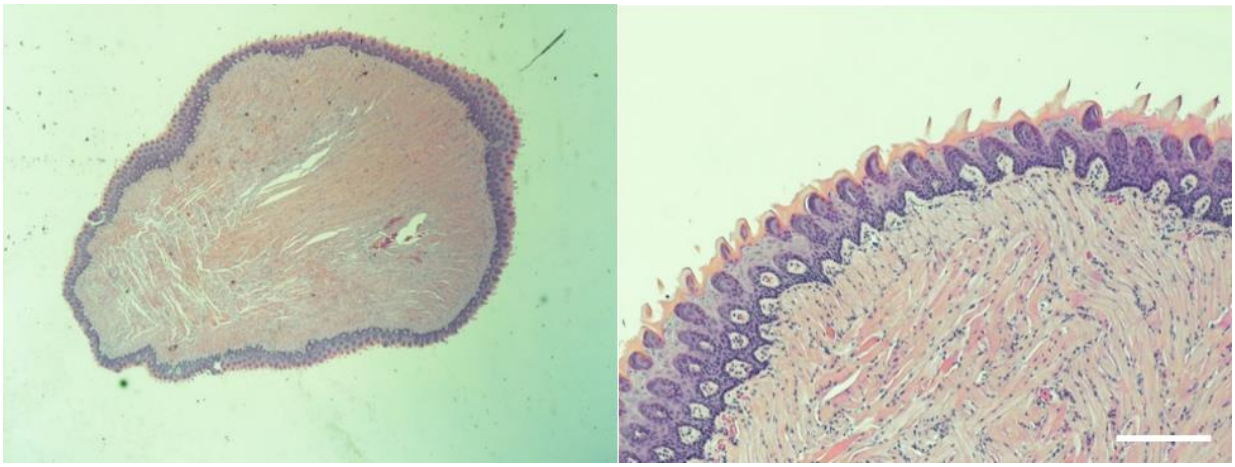

Figure 5.2.5. Histology sections of a mouse tongue at 4x and 20x magnification, left and right panels, respectively. Scalebar = 500 μm.

A normal mouse tongue was sent in for histology analysis using H&E staining and the results were presented in **Figure 5.2.5**. The vertical sections show the tongue as mainly muscle covered by filliform papillae and fungiform papillae.

5.3 Conclusion and limitations

As expected, the LS-DAC is capable of providing images with cellular detail at shallow depths for both intravenous and topically stained fresh biological specimens. The imaging contrast is higher in specimens in which the fluorescence was introduced through the circulatory system than topically.

The nature of the tissue, the chemical and photo-stability of the fluorescence agent, staining procedures, and camera exposure all play a role in determining the imaging quality of the microscope system. The staining procedures described above worked well with the imaging conditions described above; however, the procedures will need to be modified should the imaging conditions change, for example, if the desired imaging depth is beyond 200 μm to ensure proper dye penetration. The exposure time becomes critical when working with a fluorescence agent that is suboptimal in quantum efficiency. A long exposure time increases the likelihood of photobleaching and photo-damaging to the samples, while a short exposure time could lead to insufficient fluorescence signal and thereby poor imaging quality.

A previously mentioned, LS-DAC imaging depth is limited to superficial layers of the tissue. The anatomical details shown in histopathology sections (**Fig. 5.2.5**) included the muscles beyond the papillae layers. In its current form, the LS-DAC is not able to image beyond the filliforms to gain structural information of the skeletal muscles.

Chapter 6. *In vivo* Fluorescence Imaging of Biological Specimens

While *ex vivo* imaging of tissue usually provides sufficient information for histopathology diagnosis, there is invaluable information about dynamic changes in the biological specimen that can only be observed under *in vivo* settings.

Previously, tissue imaging experiments using the LS-DAC were performed in the stage-scanning format. While relatively convenient for imaging excised tissue, stage-scanning is limited in speed, where the maximum speed must not result in the accidental displacement or removal of the specimens from the sample stage. The limited imaging frame rate (~1 – 2Hz) for the stage-scanning setup cannot allow for imaging of motion, which is important in *in vivo* imaging conditions. To address this issue, we modified the LS-DAC setup (**Fig 6.1.1**) to utilize galvo mirror-scanning instead of stage-scanning to enable video-rate imaging (> 10Hz).

6.1 Modification to the optical setup

The major difference between the video-rate LS-DAC and the previous LS-DAC setup is the scanning mechanism. A galvo scanning mirror (Cambridge Technologies), driven by a custom LabVIEW VI (National Instruments), is used to scan the confocal line along the x-axis. The same VI is used to control the scanning field-of-view (FOV) during the experiments by controlling the scanning angle of the galvo.

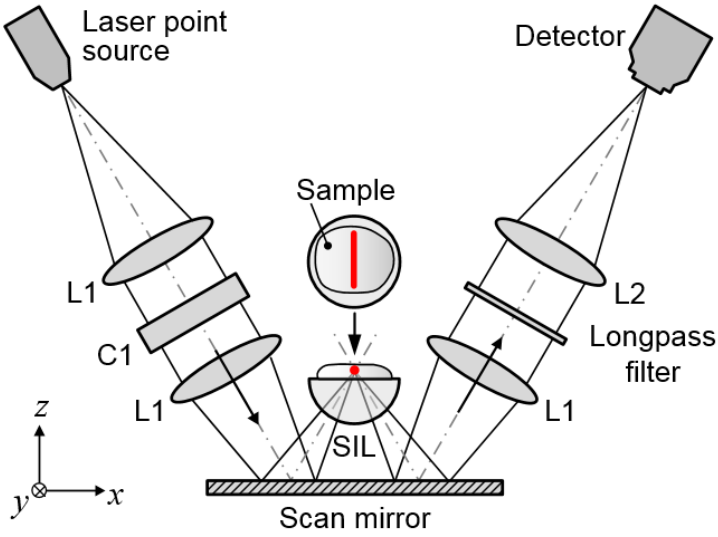

Figure 6.1.1 Optical setup of LS-DAC

In addition, a 488-nm diode laser (Coherent Inc.) is used instead of the 660-nm diode laser used in previous imaging experiments. A longpass fluorescence filter (Semrock, FF01-496/LP-25) is inserted into the collection arm of the LS-DAC setup to prevent the reflected laser light at ~488nm from being collected by the sCMOS. Individual confocal image frames are stitched

together in a line- by-line fashion using a custom MATLAB script (MathWorks) and the image stacks are rendered into videos using ImageJ (NIH).

6.2 *In vivo* fluorescence imaging of mouse ear vasculature

In vivo small animal imaging

Fluorescein isothiocyanate (FITC)-conjugated Dextran (Sigma Aldrich, FD2000S, 2000kDa, 10 mg/mL) was injected retro-orbitally into anesthetized mice to highlight their brain vasculature. The mice were anesthetized with a Ketamine/Xylazine cocktail (10 mg/mL Ketamine, 1mg/mL Xylaxine) via intraperitoneal injection at 10 mL/kg body mass. They were then placed onto a custom-made holder for the LS-DAC and the vasculature in their ears was imaged. The animals remained under anesthesia during the imaging experiments and were immediately sacrificed upon the completion of the experiments.

As mentioned briefly in Chapter 5, the injection of anesthesia and dye material needs special attention as it is crucial to the animals' survival during the imaging experiment. In addition, the recipe for the anesthesia cocktail vary depending on the literature source. For example, under-dosing the animal will cause disruption of experiments, possible destruction of valuable optical setup, and no to mention undue stress to the experimental subject. If the Xylazine concentration is too high in the cocktail, the animal will suffer from bradycardia (very low resting heart rate) and has a high probability of dying during the experiment. On the other hand, if the Ketamine concentration is too high, the animal will exhibit sporadic muscle twitch while unconscious; this will be problematic since the scale of movement is often on the order of millimeters, which will move the imaging specimen off the sample stage. As a general rule of working with small animals for *in vivo* experiments, anesthetics dosage should be determined accurately before proceeding with large number of animal subjects.

Image collection

In this study, fluorescence imaging of *in vivo* bloodflow was performed on anesthetized mice. The experiments were performed at two frame-rates. At a slow rate of 10 – 12 fps, a field of view of ~500 x 500 μm is achieved. At 30 fps, a smaller field of view of ~150 x 500 μm is achieved. The camera exposure is set at 167 - 200 μs.

In low camera exposure settings, the sCMOS camera is able to read out 5000 – 6000 camera-frames per second. Each individual confocal image frame can be stitched together with ~500 camera-frames (or ~150 camera-frames at the fastest setting), allowing for 10 – 12 fps imaging for a ~500x500 μm field-of-view and 30 fps video-rate imaging for a small ~150x500 μm field-of-view.

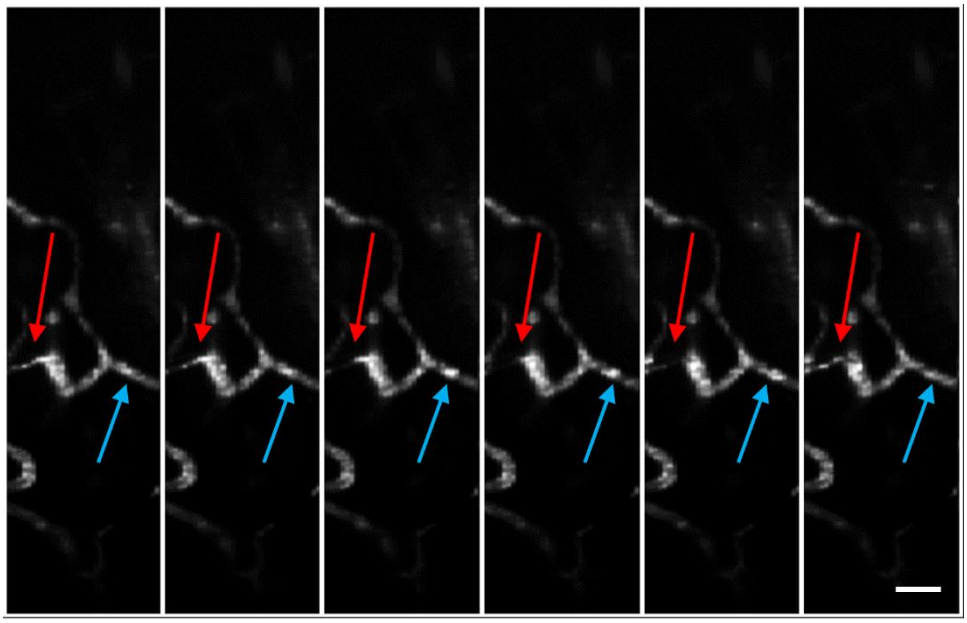

Figure 6.2.1 Selected video frames from *in vivo* imaging with small FOV (~150x500 µm) at 30fps. Red and blue arrows mark the regions where blood flow is clearly visualized in fluorescence. Scale bar = 50 µm

In the 30 fps images (**Fig. 6.2.1**), the clearing and filling of individual vessels in the region of the mouse ear capillary bed imaged can be visualized. The momentary occlusion of the vessel indicated by the red arrow and the immediate clearing is shown.

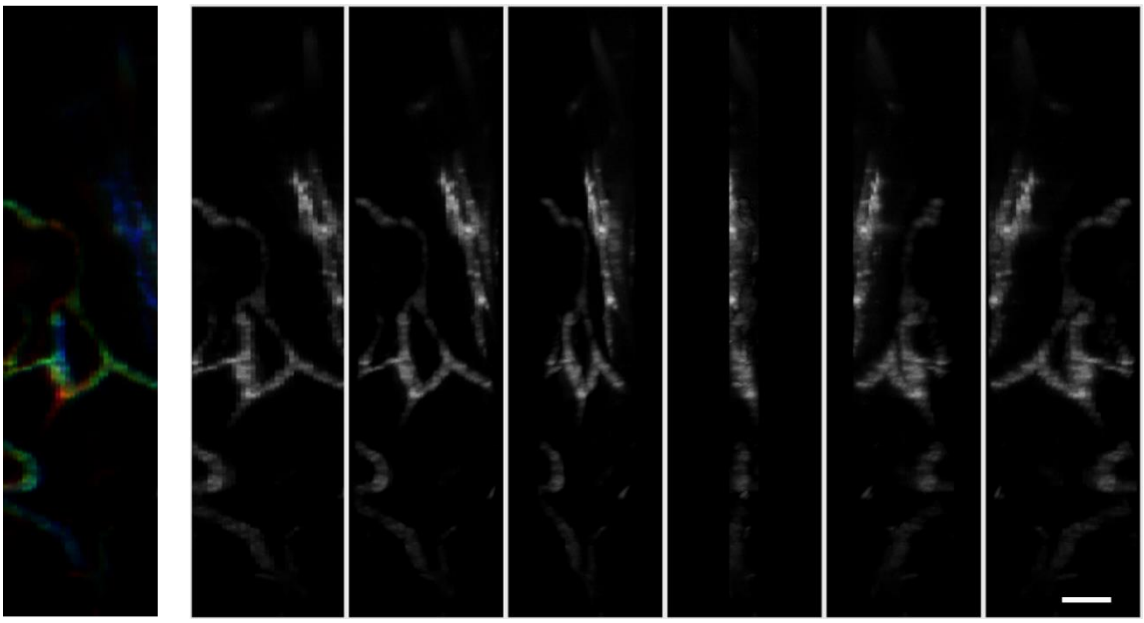

Figure 6.2.2 3D projection (left most) of the blood vessel shown in **Fig 6.2.1** with color encoding depth (blue to red in increasing depth spanning ~30 µm. Right image panels show the volume as it rotates in space. Scale bar = 50 µm

Since the confocal slit is applied digitally instead of physically, some limited 3D information can be gained by the LS-DAC without scanning in the z-direction (detailed in Chapter 7), as shown in **Fig. 6.2.2**. This is a convenient way quickly survey not only the region of interest, but the volume around the ROI. The ability to rapidly survey a 3D volume proximal to the slice of interest can potentially provide important information in medical diagnostics.

With a FOV of 500x500 µm, the imaging frame rate is decreased to 10-12 fps (**Fig. 6.2.3**). The blood flow can still be visualized but only very subtle changes between subsequent frames, and the bloodflow visualized in the video clip resemble visual flicker instead of clear passage of individual blood cells.

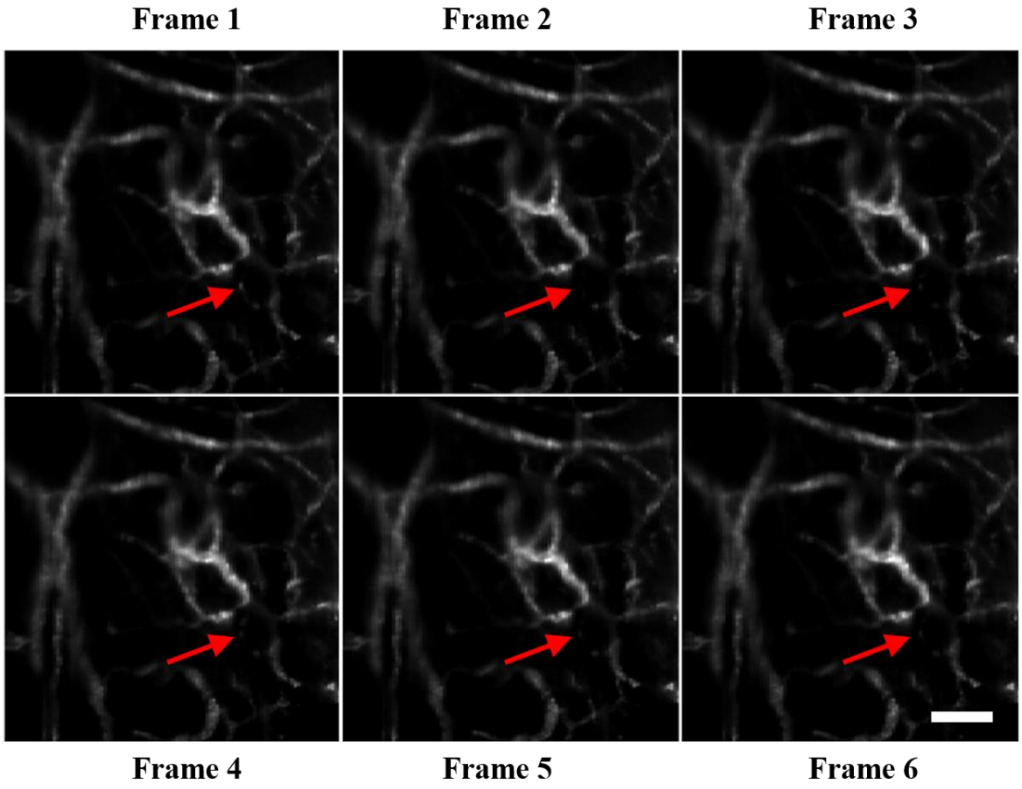

Figure 6.2.3 Selected video frames from *in vivo* imaging with full FOV (~500x500 µm) at 12 fps. Red arrows mark the regions where blood flow is visualized in fluorescence. Scale bar = 100 µm

6.3 Conclusion and limitations

This is the first time *in vivo* video-rate imaging at 30fps was achieved on the LS-DAC setup, a significant progress in the development of the DAC system. The change in scanning mechanism did not affect the imaging performance of the LS-DAC. The video-rate confocal images retained the expected resolution and contrast. No significant photo-bleaching was noted during the experiments; however, intravenous extravasation of the FITC dextran was noted when a subject was imaged for longer than 20 minutes.

While blood flow can still be visualized at full frame, the flow rate was too rapid in the capillaries (~2 – 3.5 mm/s[53]) to be visualized with cellular clarity at 10-12 fps. The labeling of blood vessel by fluorescent dextran does not specifically label individual blood cells, making the monitoring of blood flow difficult; however, when monitoring disease progression, the size, clustering, and permeability of the vasculature is arguably sufficient. Should there be a need for tracking individual blood cell movement, targeted fluorescent agents should be used instead of dextrans.

Aside from constraints in optical designs, the maximum achievable imaging speed also depends on the sCMOS read-out speed, the I/O speed of the acquisition computer, and the efficiency of the frame-grabbing algorithm. Since the volume of data streamed to disc was large, video clips of only a few seconds in length were obtained. The current workstation struggles to keep up with the sCMOS's data acquisition rate. This contributes significantly to the unstable data read/write, which often results in a lagged or truncated image. In addition, the scanning galvo mirror is controlled by a separate LabVIEW script than the stitching algorithm to generate the individual frames. With a faster workstation, both scanning and frame-grabbing functions can potentially be included in a single program, which would significantly increase the user-friendliness of the platform.

Ultimately, the I/O of the sCMOS camera also limits the imaging field-of-view and the frame-rate. If the sCMOS is capable of readout at > 30 kHz, higher frame-rates can be achieved without sacrificing the FOV. As the sCMOS used for acquisition is the current state-of-the-art technology, higher read-out rates will be expected in future models of the sCMOS. It is, however, worth noting that most human eyes cannot distinguish the flicker rate above 30 fps, so video-rate of higher than 30 fps will not be necessary for real-time imaging.

Chapter 7. Sheet-scanned Dual-axis Confocal (SS-DAC) using Deconvolution

7.1 Background and motivation

In many confocal systems, a physical pinhole or confocal slit is utilized as a spatial filter. Previously in our work when using a sCMOS detector for LS-DAC microscopy, we applied a digital confocal slit and discarded the information from the pixels outside of this slit. However, we recognize that there is still relevant information in the pixels that were previously discarded. Therefore, in this study, we analyzed the entire image volume visualized by the sCMOS during sheet-scanned acquisition (**Fig. 7.1.1c**) in order to improve a single *en face* confocal image at the center of the volume.

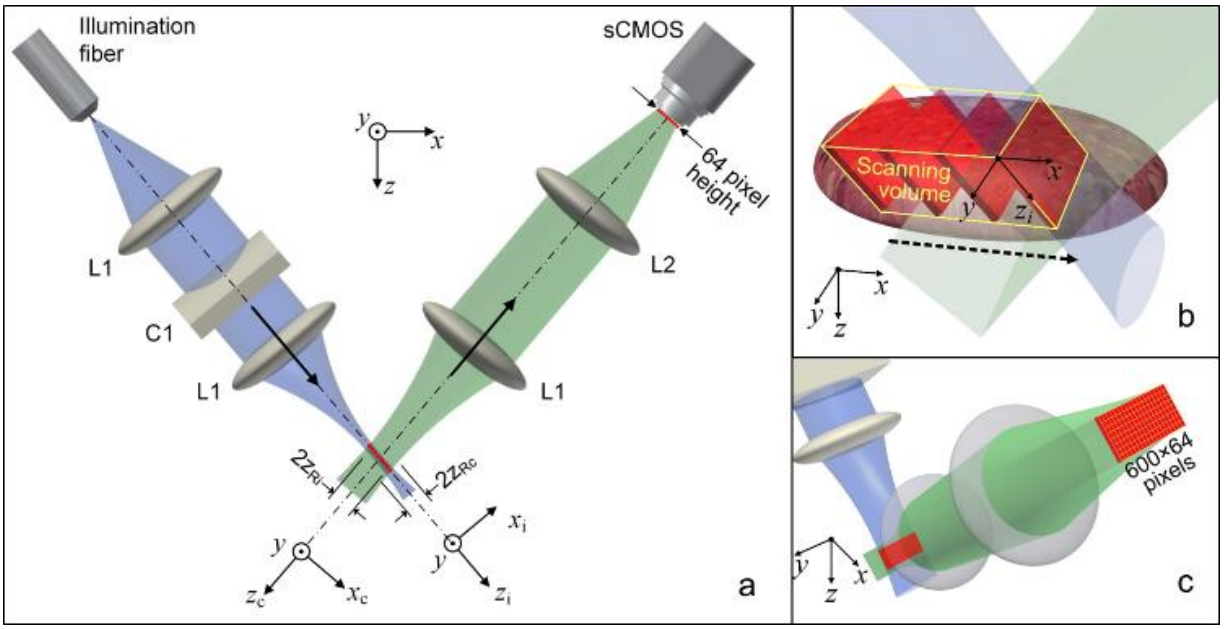

Figure7.1.1[3] (a) Schematic of the tabletop SS-DAC microscope system. The confocal parameter, $2z_R$, of the low-NA intersecting beams (illumination and collection beams) is indicated. (b) Zoomed-in view of the 3D volume imaged within the sample. (c) Zoomed-in view of the short (64-pixel tall) oblique light sheet collected by a sCMOS camera.

In contrast to the more traditional deconvolution methods that are used as an alternative to confocal microscopy to improve resolution and image contrast, here we seek to improve a confocal image by leveraging information outside of a confocal slit (through deconvolution) prior to applying a digital slit. This is somewhat analogous to recent efforts, such as pixel-reassignment, which utilize detector arrays and image processing for rapid enhanced-resolution confocal imaging of biological samples[54-57]. In this study, we explore the use of Richardson-Lucy, a restorative deconvolution algorithm, on the sheet-scanned image volume before applying a confocal slit to generate an enhanced confocal image, a process we call sheet-scanned dual-axis confocal (SS-DAC) microscopy. We compare the fluorescence imaging performance of LS-DAC, SS-DAC with

sequential 2D deconvolution, as well as SS-DAC with 3D deconvolution. Sequential 2D deconvolution refers to performing deconvolution on each of the individual oblique light sheets imaged by the sCMOS camera, stitching together the deconvolved light sheets to construct an image volume, and then applying a digital confocal slit to retrieve a single 2D *en face* SS-DAC image. 3D deconvolution refers to performing deconvolution on the entire scanned volume prior to applying a digital confocal slit at the center of the volume to retrieve a single 2D *en face* SS-DAC image. With SS-DAC, we aim to improve the contrast (signal-to-background ratio), and resolution compared to a standard LS-DAC microscope.

Figure 7.1.1 provides a schematic of the SS-DAC system, which utilizes the same optical setup as a LS-DAC system described previously [58]. Note that the central 32 pixels imaged by the sCMOS camera in the x_c direction are acquired within the confocal parameter (twice the Rayleigh range) of both the illumination ($2z_{Ri}$) and collection ($2z_{Rc}$) beam paths and can therefore be approximated as "in focus".

7.2 Richardson-Lucy Deconvolution

An image acquired by an optical system can be defined as:

$$img(x,y,z) = \iiint_{-\infty}^{\infty} psf(x-x', y-y', z-z') * obj(x',y',z')dx'dy'dz'$$

or simply as a convolution:

$$image = object \otimes psf$$

In short, an image is created by the blurring of an object (sample) by the point-spread-function (PSF) of an optical system [59, 60]. The concept of deconvolution assumes that if the image is the result of an object convolved with a PSF, then it is possible to acquire an estimate of the true object if the observed object (image) and the system PSF are known.

Deconvolution algorithms require an input of a point-spread-function (PSF), which describes the 3D (or 2D) impulse response of the optical system to a point source. The PSF can be modeled computationally or measured empirically.

All image processing was performed using MATLAB (Mathworks Inc, Natick, MA). A standard Richardson-Lucy (RL) deconvolution algorithm was used in both the 2D and 3D cases for 10 iterations each. The RL algorithm has been developed and studied extensively in the past [61-64]. The basic steps can be summarized as:

0. Obtain initial estimate $\hat{o}$

For each iteration:

1. Calculate relative blur: $\hat{\imath}^{(k)} = \hat{o}^{(k)} \otimes psf$
2. Find error term: $\frac{image}{\hat{\imath}^{(k)}}$
3. Update estimate: $\hat{o}^{(k+1)} = \hat{o}^{(k)} \frac{image}{\hat{\imath}^{(k)}}$
4. Apply non-negative constraint:
   if $\hat{o}^{(k+1)}<1$, then $\hat{o}^{(k+1)}=0$
5. Increment iteration: k = k+1

In plain terms, first, an initial estimate of the true object as a starting point. This estimate is largely arbitrary and dependent on the scripting/programming language or software used. In MATLAB, the initial estimate is set as an arbitrary uniform 50% grey image.

For each iteration, the estimate is convolved with the PSF provided by the user and the difference between the estimated image and the actual image is calculated. Then the estimate image is updated with the error term found. The program then checks for any negative pixel values post-estimate-update, and sets those pixels to 0. The algorithm will run as many times as the user indicates.

7.3 PSF measurement

7.3.1 FRED modeling of PSF

Theoretically-modeled PSF: Diffraction modeling was performed using FRED (Photon Engineering, Tucson, AZ), a commercial software. The optical setup is identical to the one used for Monte-Carlo simulation of the system. The settings in FRED were adjusted to disregard scattering calculations and perform diffraction simulations. The modeled system was identical to the experimental tabletop LS-DAC system and utilized a small (250 nm x 250 nm) Lambertian reflective surface as a point target. The PSF was obtained by recording the signal on a simulated detector array (0.1 micron spacing) as the point target was translated laterally in the *x* direction.

7.3.2 Fluorescence agarose phantom

Experimental PSF: Sub-resolution (250-nm diameter) fluorescent beads (Ex/Em: 660/680, Invitrogin F-8807) were sparsely embedded into a 1.5% agarose solution. This was done by dissolving the agarose powder (Fisher Scientific, BP160) at 1.5% by weight in a buffer at physiological pH. 1x PBS (Invitrogen, 10010-023) was used in our experiments. (TRIS buffer is also a common choice.) The buffer was heated to boiling and cooled for a few seconds before the agarose powder was added. This step is important as the agarose will "burn" if the solvent is too hot (>90°C) and will not form a gel.

The sub-resolution fluorescent beads were added into the dissolved agarose solution. The temperature of the solution should not exceed 85°C because the fluorescent beads will melt (per verbal communication with vendor technical support). The bead and agarose mixture were stirred

continuously while the gelling mold was being prepared. The ideal gelling temperature is 50 – 55°C to ensure gel consistency and to avoid inclusion of air bubbles (occurs at < 50°C).

A metal mold was heated to approximately the same temperature of the agarose-bead mixture. The mixture was poured into the mold and carefully cooled until gel formed. Note, this process can be sped-up by putting the mold with the agarose-bead mixture into the fridge (4°C), NOT the freezer (-20°C), for a few minutes. If time is not a factor in the experiment, it is best to allow the gel to cool and form naturally to prevent undesired inconsistency in gelling and the formation of bubbles in the gel.

The solidified agarose gel was imaged in three dimensions, using the sCMOS camera as a detector, by translating the sample in the *x* direction only. Individual beads centered at the focal plane were located within the images and their 3D PSFs were obtained. For a 2D PSF, individual sCMOS image frames (oblique light sheets) were chosen in which a fluorescent bead was centered within the image.

Figure 7.3.1 provides a comparison of an experimentally measured as well as a simulated intensity PSF of the LS-DAC system, showing good agreement.

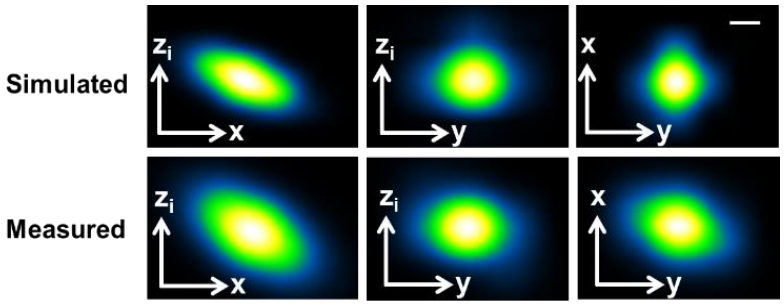

Figure 7.3.1[3]. Comparison of the experimentally measured and numerically modeled PSFs. Scale bar = 1 μm.

7.4 Fluorescence sample preparation

The tissue preparation for SS-DAC measurements are identical to that of LS-DAC, as detailed previously in Chapter 5.

In brief, for vasculature imaging, fluorescent conjugated dextran was injected retro-orbitally into the sinus capillary bed of anesthetized mice. The mice were sacrificed within 30 seconds of dye injection and fresh brain tissue excised and imaged without further processing.

For imaging of mouse duodenum and tongue, the tissue specimens were excised and stained topically with methylene blue for 15 minutes and thoroughly rinsed with isotonic buffer before imaging. No further processing was done on the excised tissues.

7.5 Results and discussion

In this feasibility study, we acquired 64-pixel-tall oblique light-sheets (corresponding to 60 μm within the sample along the x_c axis). Although this 64-pixel-tall dimension extends slightly beyond the confocal parameter of the illumination beam, $2z_{Ri} \sim 30$ μm, only the central pixels

(within the confocal parameter) are of value once the confocal slit is applied to the center of the image volume. In addition, prior to deconvolution, a Hanning window is applied to each short light sheet to taper the edges of the 64-pixel-long dimension in order to minimize deconvolution artifacts from sharp (high-frequency) edges. Future work will evaluate the SS-DAC method with smaller subarrays at a higher acquisition rate. For example, the smallest region of interest that our sCMOS detector (Orca Flash 4.0 v2, Hamamatsu Inc.) can acquire in its fastest acquisition mode (~25 kHz) is an 8-pixel-tall rectangular array.

SS-DAC with sequential 2D deconvolution: Each 64-pixel tall oblique light sheet was deconvolved using the 2D PSF obtained previously. A 3D image volume was stitched together with the deconvolved 2D slices. A confocal slit (3-pixel wide) was then applied to the center of the deconvolved image volume to obtain the final confocal image.

SS-DAC with 3D deconvolution: The image volume was stored in a 3D matrix and deconvolved with the 3D PSF obtained previously. A confocal slit (3-pixel wide) was then applied to the center of the deconvolved image volume to obtain the final confocal image.

To directly compare the performance of LS-DAC and SS-DAC, we performed fluorescence microscopy of fresh mouse brain vasculature, intestine, and oral tissues.

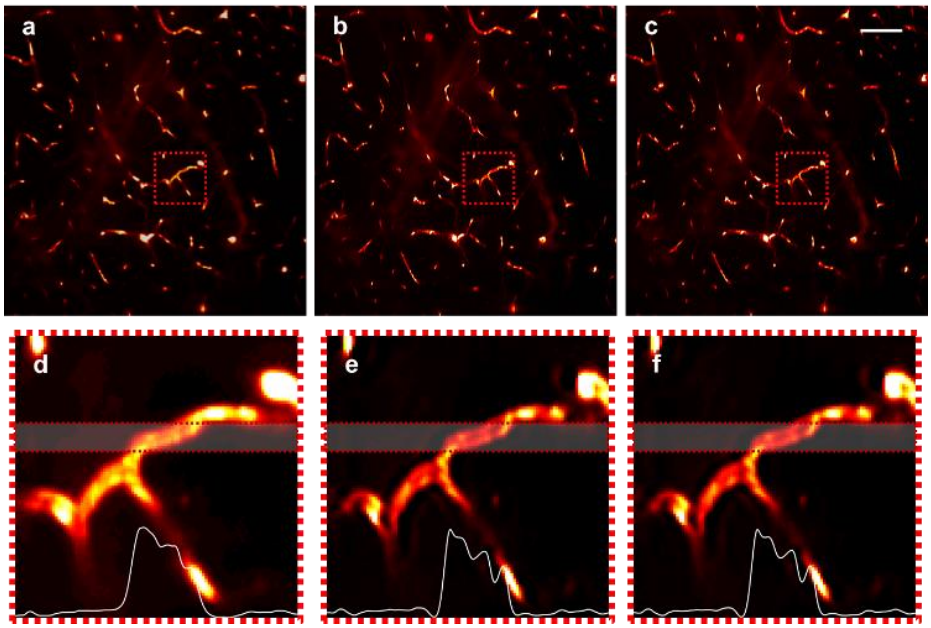

Figure 7.5.1[3]**.** A comparison of fluorescence images of mouse brain vasculature (depth ~100 µm) using (a) LS-DAC, (b) SS-DAC with sequential 2D deconvolution, and (c) SS-DAC with 3D deconvolution, presented with line profiles. The zoomed-in views of the regions outlined in (a-c) are presented in panels (d-f) respectively. Average line profiles from the highlighted region in (d-f) are shown at the bottom of each panel. Scale bar = 100 µm.

Results from fluorescence imaging of mouse brain vasculature are shown in **Fig. 7.5.1** when using SS-DAC with deconvolution (both 2D and 3D) in comparison to LS-DAC microscopy. In this case, since AF647-Dextran is injected to specifically label the brain vasculature, there is minimal background fluorescence, thus establishing a relatively high-contrast baseline condition for SS-DAC and LS-DAC microscopy (**Fig. 7.5.1**). Therefore, although the improvement in

resolution is evident (i.e., the vascular details appear sharper in the deconvolved images), the improvement in contrast is not dramatic.

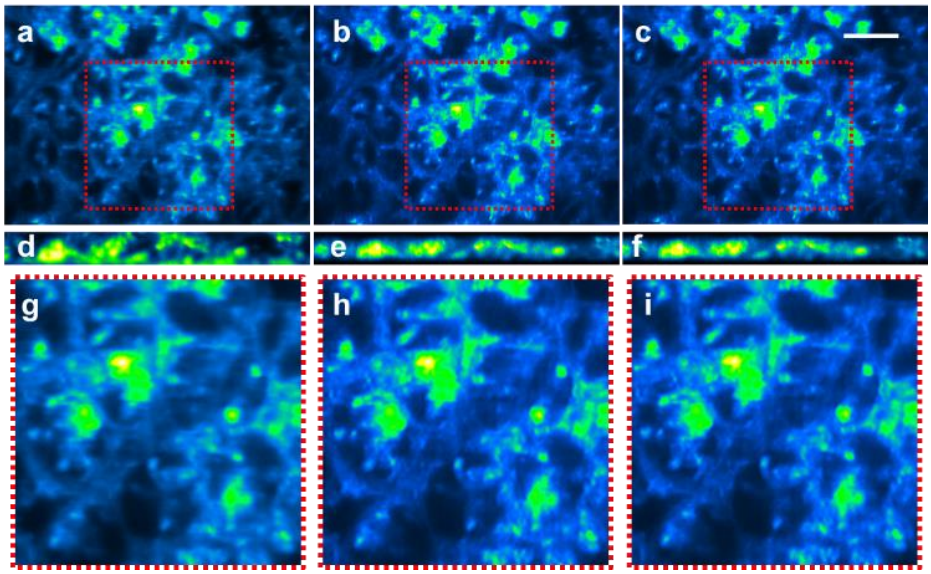

Figure 7.5.2[3] A comparison of mouse duodenum (depth ~100 µm) nonspecifically stained with Methylene Blue and fluorescently imaged using a) LS-DAC, (b) SS-DAC with sequential 2D deconvolution, and (c) SS-DAC with 3D deconvolution. Oblique light sheets, obtained at the center of the image volume, are shown in (d-f). The zoomed-in views of the regions outlined in (a-c) are presented in panels (g-i) respectively. Scale bar = 100 µm.

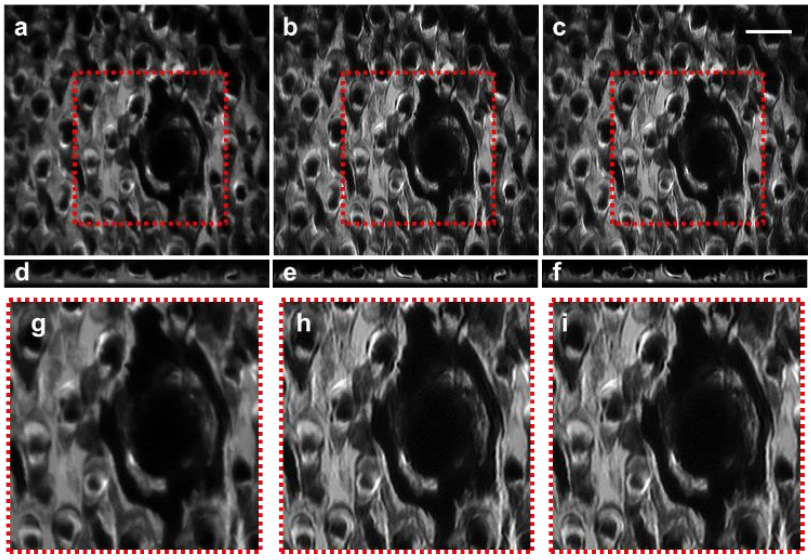

Figure 7.5.3[3] A comparison of mouse tongue (depth ~50 µm) stained non-specifically with Methylene Blue and fluorescently imaged using a) LS-DAC, (b) SS-DAC with sequential 2D deconvolution, and (c) SS-DAC with 3D deconvolution. Oblique light sheets, obtained at the center of the imaging volume are shown in (d-f). The zoomed-in views of the regions outlined in (a-c) are presented in panels (g-i) respectively. Scale bar = 100 µm.

In the case of intestinal tissues, MB was used to nonspecifically stain all luminal structures, resulting in worse contrast for the LS-DAC images. The features of the duodenal glands appear sharper, and image contrast is moderately improved, in the SS-DAC images (**Fig. 7.5.2**).

LS-DAC images of mouse oral tissue (tongue) reveal fungiform and filiform papillae (**Fig. 7.5.3**). The outlines of the numerous filiform papillae surrounding the fungiform papillae are sharper in the SS-DAC images.

7.6 Conclusion and limitations

SS-DAC using both 2D and 3D deconvolution methods show similar levels of improvement compared to LS-DAC images. In addition, the deconvolution processing time is approximately the same for both sequential 2D deconvolution (performed over an entire image volume) and 3D deconvolution. The RL algorithm is designed to perform well under relatively high SNR conditions. Results from our experiments confirm that the RL deconvolution algorithm is suitable for processing images obtained under our experimental conditions, i.e. at relatively shallow imaging depths (< 150 μm).

We combine a pseudo-light-sheet microscopy approach with digital image processing using the RL restorative deconvolution algorithm prior to applying a confocal slit and acquiring a final confocal image, a technique referred to as sheet-scanned dual-axis confocal (SS-DAC) microscopy. We are able to improve the resolution in our images compared to images from a basic LS-DAC setup with modest improvements in image contrast.

This approach is potentially very useful in low-signal conditions, where it is commonplace to increase the size of the confocal pinhole or slit to improve sensitivity, but at the cost of resolution and contrast.

To explore this idea, the size of the confocal slit was opened from 3-pixel to 5-pixel wide. The new confocal image is obtained and processed with 2D and 3D deconvolution. The results are shown below for topically stained mouse tongue and duodenum.

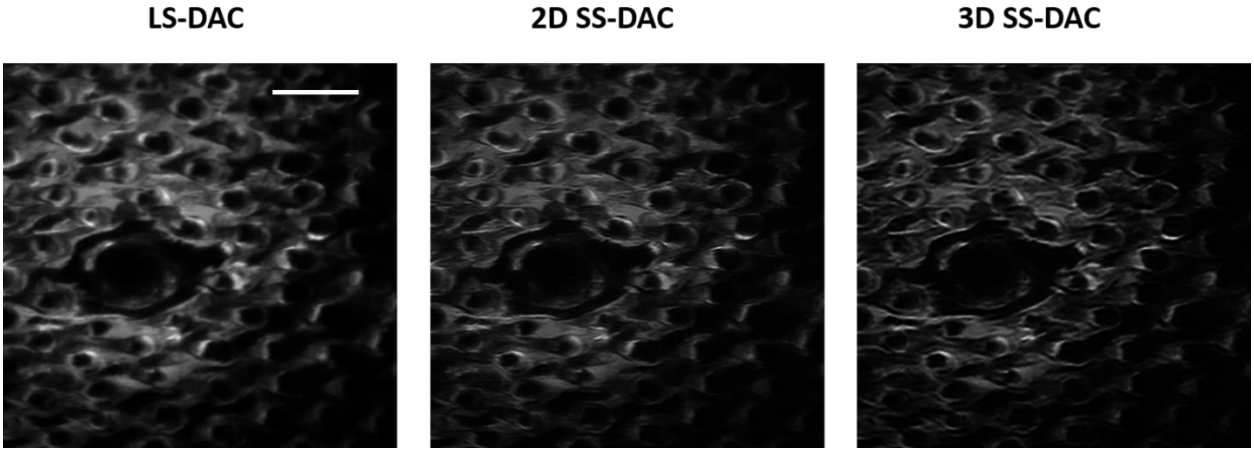

Figure 7.6.1. Mouse tongue imaged with a larger confocal slit (scalebar = 100 μm)

In the images of topically stained mouse-tongue (**Fig. 7.6.1**), there is obvious loss of resolution in the LS-DAC image when the confocal slit is further opened, as expected. Through

the deconvolution process, some resolution loss was compensated and the sharpness of the images returned. Similar observations can be made regarding the images for mouse duodenum (**Fig. 7.6.2**).

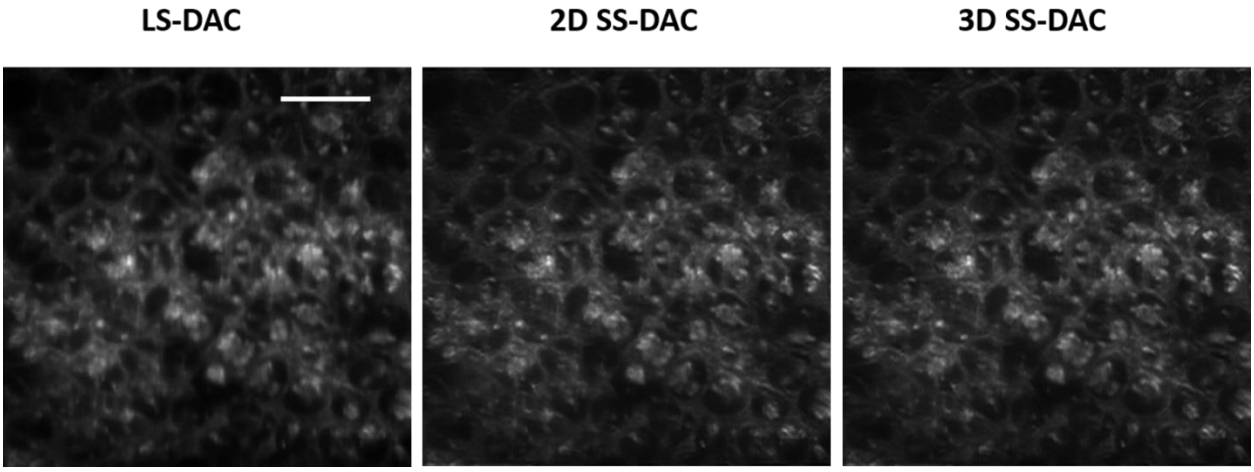

Figure 7.6.2. Mouse duodenum imaged with a larger confocal slit (scalebar = 100 μm)

In this study, we used one of the simplest implementations of the RL-deconvolution algorithm. For more complicated implementations, such as blind deconvolution, the PSF is estimated by the algorithm rather than provided by the user. In such cases, the users would also not define the number of iterations the algorithm should run. The algorithm will have a noise analysis segment, often customized by the programmer, which determines when the program will terminate (e.g. when the noise distribution is approximately Poisson, indicative of shot noise floor). The complexity of the algorithms also add to the computational cost of the procedure.

We are exploring the use of SS-DAC microscopy to restore the loss of resolution and contrast resulting from the use of a wide confocal pinhole/slit. It is both comforting and discouraging when an established pathologist, through verbal communication at a conference, informed the author that the LS-DAC images contained sufficient details for a trained pathologist to distinguish tissue types and structures; however, we will continue to explore new ways to improve SS-DAC, particularly to speed up the algorithm for potential real-time use.

Chapter 8. Conclusion and Future work

The goal of developing an optical-sectioning microscopy modality is to be able to maximize the imaging depth, speed, spatial resolution, contrast, and field-of-view. We acknowledge the impracticality of maximizing all the aforementioned parameters in one optical setup. Instead, we have, and will continue to be focused on balancing the tradeoffs between these parameters to optimize various designs. In this thesis, we explored a few of many facets of optical design and development on a DAC platform, with a focus on imaging speed.

Within the scope of this thesis, we have performed theoretical calculations and simulations for a table-top prototype of a line-scanned DAC microscope. We have compared the imaging performance of the LS-DAC to our existing PS-DAC prototype and have demonstrated comparable imaging performance at shallow depths[2]. In addition, the prototype was able to image with subcellular resolution (<5 μm) at video-rate up to 30 fps in a relatively small field-of-view [manuscript in preparation].

We have also developed accessories to aid the characterization[4], contrast enhancement[65] (not detailed in this thesis), and image processing[3] of the DAC setup. The workstation associated with the current LS-DAC setup is in the process of being upgraded for faster I/O speed capable of accommodating the read-out speed of the camera smoothly. This could potentially enable frame-rates above 30 fps, which can be useful for tracking rapid intracellular changes such as the cytosolic calcium transients in excitable cells with the aid of appropriate fluorescence dyes.

The scope of this thesis only explored a few aspects of the DAC system. Many aspects other than imaging speed are being explored in parallel at the moment. A modulated-alignment dual-axis (MAD) confocal microscope has recently been developed in our lab[66], which increases the PS-DAC's imaging depth by filtering out the background noise. We are also exploring the use of Bessel-beam illumination to alleviate the negative effects of tissue-heterogeneity-induced beam steering on the spatial resolution and contrast of DAC microscopy [Y. Chen and J.T.C. Liu, manuscript submitted].

The primary application of the microscopy research in our lab is the development of miniaturized microscopes that can be used to aid clinical diagnoses, disease monitoring, and disease treatment. There is a broad definition of what is considered a "portable" and "hand-held" microscope, ranging in size from an entire optical cart, a briefcase, or a pill. We aim to develop a miniaturized LS-DAC microscope that is similar in size to a pen or a dry-erase marker for neurosurgical guidance (NCI funding) and oral cancer detection (NIDCR funding).

The tabletop LS-DAC presented in this thesis serves as a base for prototyping and design changes for a miniature video-rate LS-DAC, which is currently under development and will potentially play an important role in point-of-care pathology in the near future.

Due to the usage of low NA lenses in the DAC systems, reflectance imaging quality can be degraded by speckle noise as it is difficult to compensate for speckle noise without significantly sacrificing the imaging resolution. While we characterized the LS-DAC in reflectance, all tissue imaging experiments were performed in fluorescence mode, taking advantage of the achromatic design of the setup. The miniaturized LS-DAC has been designed with a slightly higher NA to allow a larger pinhole, which will alleviate the negative effects of speckle noise, thus enabling the miniature LS-DAC to image in reflectance as well as fluorescence mode.

We recognize that while adding complexity to the miniature DAC design may help push the limit of what was previously achievable, the cost of the additional complexity must not drastically exceed the benefit gained in performance. A delicate balance will be maintained to ensure the design's effectiveness.

It is important to note that it is not our intention to design an imaging device to replace pathologists. These miniature microscopes will be tools available to the pathologists to more rapidly make diagnostic decisions without having to wait for tissue processing. In addition, these hand-held devices will help to triage the tissue specimens and minimize the sampling of false positive lesions, and in turn allowing the pathologists to focus on the lesions.

Ultimately, the miniature LS-DAC will be used to examine the suspicious lesions in the oral cavity to aid the diagnosis of oral squamous cell carcinoma and other relevant head-and-neck cancers.

Reference

1. J. T. C. Liu, M. J. Mandella, S. Friedland, R. Soetikno, J. M. Crawford, C. H. Contag, G. S. Kino, and T. D. Wang, "Dual-axes confocal reflectance microscope for distinguishing colonic neoplasia," Journal of biomedical optics **11**, 054019 (2006).
2. D. Wang, Y. Chen, Y. Wang, and J. T. C. Liu, "Comparison of line-scanned and point-scanned dual-axis confocal microscope performance," Optics letters **38**, 5280-5283 (2013).
3. D. Wang, D. Meza, Y. Wang, L. Gao, and J. T. C. Liu, "Sheet-scanned dual-axis confocal microscopy using Richardson-Lucy deconvolution," Optics letters **39**, 5431-5434 (2014).
4. D. Wang, Y. Chen, and J. T. Liu, "A liquid optical phantom with tissue-like heterogeneities for confocal microscopy," Biomedical optics express **3**, 3153-3160 (2012).
5. Y. Chen, D. Wang, and J. T. Liu, "Assessing the tissue-imaging performance of confocal microscope architectures via Monte Carlo simulations," Optics letters **37**, 4495-4497 (2012).
6. M. W. Lingen, J. R. Kalmar, T. Karrison, and P. M. Speight, "Critical evaluation of diagnostic aids for the detection of oral cancer," Oral oncology **44**, 10-22 (2008).
7. O. Kujan, A. M. Glenny, J. Duxbury, N. Thakker, and P. Sloan, "Evaluation of screening strategies for improving oral cancer mortality: a Cochrane systematic review," Journal of dental education **69**, 255-265 (2005).
8. T. Walsh, J. L. Liu, P. Brocklehurst, A. M. Glenny, M. Lingen, A. R. Kerr, G. Ogden, S. Warnakulasuriya, and C. Scully, "Clinical assessment to screen for the detection of oral cavity cancer and potentially malignant disorders in apparently healthy adults," The Cochrane database of systematic reviews **11**, CD010173 (2013).
9. N. L. Rhodus, "Oral cancer and precancer: improving outcomes," Compendium of continuing education in dentistry **30**, 486-488, 490-484, 496-488 passim; quiz 504, 520 (2009).
10. C. Naugler, "Practice tips. Brush biopsy sampling of oral lesions," Canadian family physician Medecin de famille canadien **54**, 194 (2008).
11. E. S. Oh and D. M. Laskin, "Efficacy of the ViziLite system in the identification of oral lesions," Journal of oral and maxillofacial surgery : official journal of the American Association of Oral and Maxillofacial Surgeons **65**, 424-426 (2007).
12. K. H. Awan, P. R. Morgan, and S. Warnakulasuriya, "Evaluation of an autofluorescence based imaging system (VELscope) in the detection of oral potentially malignant disorders and benign keratoses," Oral oncology **47**, 274-277 (2011).
13. B. Balevi, "Assessing the usefulness of three adjunctive diagnostic devices for oral cancer screening: a probabilistic approach," Community dentistry and oral epidemiology **39**, 171-176 (2011).

14. N. Bhatia, M. A. Matias, and C. S. Farah, "Assessment of a decision making protocol to improve the efficacy of VELscope in general dental practice: A prospective evaluation," Oral oncology **50**, 1012-1019 (2014).

15. C. S. Farah, L. McIntosh, A. Georgiou, and M. J. McCullough, "Efficacy of tissue autofluorescence imaging (VELScope) in the visualization of oral mucosal lesions," Head & neck **34**, 856-862 (2012).

16. D. V. Messadi, F. S. Younai, H. H. Liu, G. Guo, and C. Y. Wang, "The clinical effectiveness of reflectance optical spectroscopy for the in vivo diagnosis of oral lesions," International journal of oral science **6**, 162-167 (2014).

17. O. Brinkmann and D. T. Wong, "Salivary transcriptome biomarkers in oral squamous cell cancer detection," Advances in clinical chemistry **55**, 21-34 (2011).

18. J. M. Lee, E. Garon, and D. T. Wong, "Salivary diagnostics," Orthodontics & craniofacial research **12**, 206-211 (2009).

19. J. Chen, J. Zhang, Y. Guo, J. Li, F. Fu, H. H. Yang, and G. Chen, "An ultrasensitive electrochemical biosensor for detection of DNA species related to oral cancer based on nuclease-assisted target recycling and amplification of DNAzyme," Chem Commun (Camb) **47**, 8004-8006 (2011).

20. C. J. Koester, S. M. Khanna, H. D. Rosskothen, R. B. Tackaberry, and M. Ulfendahl, "Confocal slit divided-aperture microscope: applications in ear research," Applied optics **33**, 702-708 (1994).

21. T. Sankar, P. M. Delaney, R. W. Ryan, J. Eschbacher, M. Abdelwahab, P. Nakaji, S. W. Coons, A. C. Scheck, K. A. Smith, R. F. Spetzler, and M. C. Preul, "Miniaturized handheld confocal microscopy for neurosurgery: results in an experimental glioblastoma model," Neurosurgery **66**, 410-417; discussion 417-418 (2010).

22. K. C. Maitland, A. M. Gillenwater, M. D. Williams, A. K. El-Naggar, M. R. Descour, and R. R. Richards-Kortum, "In vivo imaging of oral neoplasia using a miniaturized fiber optic confocal reflectance microscope," Oral oncology **44**, 1059-1066 (2008).

23. M. Rajadhyaksha, S. Gonzalez, J. M. Zavislan, R. R. Anderson, and R. H. Webb, "In vivo confocal scanning laser microscopy of human skin II: advances in instrumentation and comparison with histology," The Journal of investigative dermatology **113**, 293-303 (1999).

24. S. Gonzalez, M. Rajadhyaksha, G. Rubinstein, and R. R. Anderson, "Characterization of psoriasis in vivo by reflectance confocal microscopy," Journal of medicine **30**, 337-356 (1999).

25. R. G. Langley, M. Rajadhyaksha, P. J. Dwyer, A. J. Sober, T. J. Flotte, and R. R. Anderson, "Confocal scanning laser microscopy of benign and malignant melanocytic skin lesions in vivo," Journal of the American Academy of Dermatology **45**, 365-376 (2001).

26. P. J. Dwyer, C. A. DiMarzio, J. M. Zavislan, W. J. Fox, and M. Rajadhyaksha, "Confocal reflectance theta line scanning microscope for imaging human skin in vivo," Optics letters **31**, 942-944 (2006).

27. P. J. Dwyer, C. A. DiMarzio, and M. Rajadhyaksha, "Confocal theta line-scanning microscope for imaging human tissues," Applied optics **46**, 1843-1851 (2007).

28. D. S. Gareau, S. Abeytunge, and M. Rajadhyaksha, "Line-scanning reflectance confocal microscopy of human skin: comparison of full-pupil and divided-pupil configurations," Optics letters **34**, 3235-3237 (2009).

29. B. Larson, S. Abeytunge, and M. Rajadhyaksha, "Performance of full-pupil line-scanning reflectance confocal microscopy in human skin and oral mucosa in vivo," Biomedical optics express **2**, 2055-2067 (2011).

30. Y. G. Patel, M. Rajadhyaksha, and C. A. Dimarzio, "Optimization of pupil design for point-scanning and line-scanning confocal microscopy," Biomedical optics express **2**, 2231-2242 (2011).

31. M. Rajadhyaksha, "Confocal microscopy of skin cancers: translational advances toward clinical utility," Conference proceedings : ... Annual International Conference of the IEEE Engineering in Medicine and Biology Society. IEEE Engineering in Medicine and Biology Society. Conference **2009**, 3231-3233 (2009).

32. T. D. Wang, M. J. Mandella, C. H. Contag, and G. S. Kino, "Dual-axis confocal microscope for high-resolution in vivo imaging," Optics letters **28**, 414-416 (2003).

33. J. T. Liu, M. J. Mandella, S. Friedland, R. Soetikno, J. M. Crawford, C. H. Contag, G. S. Kino, and T. D. Wang, "Dual-axes confocal reflectance microscope for distinguishing colonic neoplasia," Journal of biomedical optics **11**, 054019 (2006).

34. J. T. Liu, M. J. Mandella, J. M. Crawford, C. H. Contag, T. D. Wang, and G. S. Kino, "Efficient rejection of scattered light enables deep optical sectioning in turbid media with low-numerical-aperture optics in a dual-axis confocal architecture," Journal of biomedical optics **13**, 034020 (2008).

35. J. T. Liu, M. J. Mandella, N. O. Loewke, H. Haeberle, H. Ra, W. Piyawattanametha, O. Solgaard, G. S. Kino, and C. H. Contag, "Micromirror-scanned dual-axis confocal microscope utilizing a gradient-index relay lens for image guidance during brain surgery," Journal of biomedical optics **15**, 026029 (2010).

36. W. Piyawattanametha, H. Ra, Z. Qiu, S. Friedland, J. T. Liu, K. Loewke, G. S. Kino, O. Solgaard, T. D. Wang, M. J. Mandella, and C. H. Contag, "In vivo near-infrared dual-axis confocal microendoscopy in the human lower gastrointestinal tract," Journal of biomedical optics **17**, 021102 (2012).

37. T. R. Corle and G. S. Kino, *Confocal scanning optical microscopy and related imaging systems* (Academic Press, San Diego, 1996), pp. xv, 335 p.

38. Y. Chen and J. T. Liu, "Optimizing the performance of dual-axis confocal microscopes via Monte-Carlo scattering simulations and diffraction theory," Journal of biomedical optics **18**, 066006 (2013).

39. P. van der Zee, M. Essenpreis, and D. T. Delpy, "Optical properties of brain tissue," in *SPIE*, 1993), 454-465.

40. J. Hwang, J. C. Ramella-Roman, and R. Nordstrom, "Introduction: feature issue on phantoms for the performance evaluation and validation of optical medical imaging devices," Biomedical optics express **3**, 1399-1403 (2012).

41. T. Moffitt, Y. C. Chen, and S. A. Prahl, "Preparation and characterization of polyurethane optical phantoms," Journal of biomedical optics **11**, 041103 (2006).

42. L. Luu, P. A. Roman, S. A. Mathews, and J. C. Ramella-Roman, "Microfluidics based phantoms of superficial vascular network," Biomedical optics express **3**, 1350-1364 (2012).

43. H. Azarnoush, S. Vergnole, V. Pazos, C. E. Bisaillon, B. Boulet, and G. Lamouche, "Intravascular optical coherence tomography to characterize tissue deformation during angioplasty: preliminary experiments with artery phantoms," Journal of biomedical optics **17**, 96015-96011 (2012).

44. B. W. Pogue and M. S. Patterson, "Review of tissue simulating phantoms for optical spectroscopy, imaging and dosimetry," Journal of biomedical optics **11**, 041102 (2006).

45. S. L. Jacques, B. Wang, and R. Samatham, "Reflectance confocal microscopy of optical phantoms," Biomedical optics express **3**, 1162-1172 (2012).

46. S. Y. Leigh and J. T. C. Liu, "Multi-color miniature dual-axis confocal microscope for point-of-care pathology," Optics letters **37**, 2430-2432 (2012).

47. F. O. Fahrbach and A. Rohrbach, "Propagation stability of self-reconstructing Bessel beams enables contrast-enhanced imaging in thick media," Nature communications **3**, 632 (2012).

48. F. O. Fahrbach and A. Rohrbach, "A line scanned light-sheet microscope with phase shaped self-reconstructing beams," Optics express **18**, 24229-24244 (2010).

49. T. A. Planchon, L. Gao, D. E. Milkie, M. W. Davidson, J. A. Galbraith, C. G. Galbraith, and E. Betzig, "Rapid three-dimensional isotropic imaging of living cells using Bessel beam plane illumination," Nature methods **8**, 417-U468 (2011).

50. A. Riaz, B. Shreedhar, M. Kamboj, and S. Natarajan, "Methylene blue as an early diagnostic marker for oral precancer and cancer," SpringerPlus **2**, 95 (2013).

51. Y. W. Chen, J. S. Lin, J. H. Fong, I. K. Wang, S. J. Chou, C. H. Wu, M. T. Lui, C. S. Chang, and S. Y. Kao, "Use of methylene blue as a diagnostic aid in early detection of oral cancer and precancerous lesions," The British journal of oral & maxillofacial surgery **45**, 590-591 (2007).

52. D. Wirth, M. Snuderl, W. Curry, and A. Yaroslavsky, "Comparative evaluation of methylene blue and demeclocycline for enhancing optical contrast of gliomas in optical images," Journal of biomedical optics **19**, 90504 (2014).

53. M. Unekawa, M. Tomita, Y. Tomita, H. Toriumi, K. Miyaki, and N. Suzuki, "RBC velocities in single capillaries of mouse and rat brains are the same, despite 10-fold difference in body size," Brain research **1320**, 69-73 (2010).

54. C. J. Sheppard, S. B. Mehta, and R. Heintzmann, "Superresolution by image scanning microscopy using pixel reassignment," Optics letters **38**, 2889-2892 (2013).

55. C. B. Muller and J. Enderlein, "Image scanning microscopy," Physical review letters **104**, 198101 (2010).

56. Y. Wu, A. Ghitani, R. Christensen, A. Santella, Z. Du, G. Rondeau, Z. Bao, D. Colon-Ramos, and H. Shroff, "Inverted selective plane illumination microscopy (iSPIM) enables coupled cell identity lineaging and neurodevelopmental imaging in Caenorhabditis elegans," Proceedings of the National Academy of Sciences of the United States of America **108**, 17708-17713 (2011).

57. A. G. York, S. H. Parekh, D. Dalle Nogare, R. S. Fischer, K. Temprine, M. Mione, A. B. Chitnis, C. A. Combs, and H. Shroff, "Resolution doubling in live, multicellular organisms via multifocal structured illumination microscopy," Nature methods **9**, 749-754 (2012).

58. D. Wang, Y. Chen, Y. Wang, and J. T. Liu, "Comparison of line-scanned and point-scanned dual-axis confocal microscope performance," Optics letters **38**, 5280-5283 (2013).

59. J. R. Swedlow, "Quantitative fluorescence microscopy and image deconvolution," Methods in cell biology **114**, 407-426 (2013).

60. W. Wallace, L. H. Schaefer, and J. R. Swedlow, "A workingperson's guide to deconvolution in light microscopy," BioTechniques **31**, 1076-1078, 1080, 1082 passim (2001).

61. J. Llacer, Nunez, J, "Ghost images and feasibility of reconstructions with the Richardson-Lucy algorithm," in *Image Reconstruction and Restoration*, (SPIE, 1994),

62. L. B. Lucy, "An iterative technique for the rectification of observed distributions," Astronomical Journal **79**, 745 (1974).

63. W. H. Richardson, "Bayesian-Based Iterative Method of Image Restoration," J. Opt. Soc. Am. **62**, 55-59 (1972).

64. T. J. Holmes and Y. H. Liu, "Richardson-Lucy/maximum likelihood image restoration algorithm for fluorescence microscopy: further testing," Applied optics **28**, 4930-4938 (1989).

65. D. Wang, Y. Chen, S. Y. Leigh, H. Haeberle, C. H. Contag, and J. T. Liu, "Microscopic Delineation of Medulloblastoma Margins in a Transgenic Mouse Model Using a Topically Applied VEGFR-1 Probe," Translational oncology **5**, 408-414 (2012).

66. S. Y. Leigh, Y. Chen, and J. T. Liu, "Modulated-alignment dual-axis (MAD) confocal microscopy for deep optical sectioning in tissues," Biomedical optics express **5**, 1709-1720 (2014).